8-2020

Paleoenvironment Reconstruction of the Eocene Southeastern Tethys Using Geochemistry of Sedimentary Rocks

Liliana Calderón Convers

ABSTRACT

PALEOENVIRONMENT RECONSTRUCTION OF THE EOCENE SOUTHEASTERN TETHYS USING GEOCHEMISTRY OF SEDIMENTARY ROCKS

By Liliana Calderón Convers

The Early Eocene hyperthermals are a series of transient global warming events that occurred between 54.09 and 52.63 Ma, and are considered as ancient analogues for future climate change. These hyperthermal events are well studied in the deep sea sites, but have not been investigated in the eastern Tethys Ocean. Here, we report new major and trace element geochemistry and stable carbon isotope data of the Early Eocene strata deposited in a shallow marine foreland basin prior to the main stage of India-Asian continent collision at Qumiba section in the Tingri County, southern Tibet. These geochemical data are used to reconstruct the paleoenvironment and past carbon cycle dynamics in the Early Eocene. The collision of India with Asia continent led to the formation of the Himalayas and the demise of the Tethys Ocean. This tectonic event played a significant role in the paleotopography, paleoceanography and paleoclimate of the southeastern Tethys. The youngest marine sediments (Enba Formation and Zhaguo Formation) represent the closure of the Tethys Ocean, and suggest an age of 53.67 to 52.63 Ma. Major element geochemistry and weathering indices indicate that the Eocene southeastern Tethys may have experienced periodic pulses of nutrient-rich detrital sediments, weathering supplies and the development of hypoxia in the water column, consistent with the warm and humid climate in the Early Eocene.

Keywords: Paleoenvironment, Eocene Thermal Maximum 2 (ETM 2), Qumiba section, geochemistry, Carbon, Nitrogen stable isotopes.

MONTCLAIR STATE UNIVERSITY

PALEOENVIRONMENT RECONSTRUCTION OF THE EOCENE SOUTHEASTERN TETHYS USING GEOCHEMISTRY OF SEDIMENTARY ROCKS

by

LILIANA CALDERON CONVERS

A Master's Thesis Submitted to the Faculty of

Montclair State University

In Partial Fulfillment of the Requirements

For the Degree of

Master of Science

August 2020

College of Science and Mathematics

Department Earth and Environmental Studies

Thesis Committee:

[redacted]

Thesis Sponsor Dr. Ying Cui

[redacted]

Committee member Dr. Sandra Passchier

[redacted]

Committee member Dr. Matthew Gorring

PALEOENVIRONMENT RECONSTRUCTION OF THE EOCENE SOUTHEASTERN TETHYS USING GEOCHEMISTRY OF SEDIMENTARY ROCKS

A THESIS

Submitted in partial fulfillment of the requirements

for the degree of

Master of Science

by

LILIANA CALDERÓN-CONVERS

Montclair State University

Montclair, NJ

2020

Acknowledgements

For me geochemistry is a fascinating subject; the study of stable isotopes represented a complex subject, comparable to learning a new language. After having reached this milestone, I am deeply honored with my remarkable professors who introduced me to these subjects and all knowledge I acquired, namely through the use of analytical methods.

It has been a privilege to work with my thesis advisor Dr. Ying Cui from the Department of Earth and Environmental Sciences at Montclair State University. I would like to thank you for your patience, availability, dedication, and commitment with my thesis. Additionally, to my thesis committee members: Dr. Sandra Passchier, many thanks for always being available, eager to help, and for stimulating discussions. Dr. Matthew Gorring, I would like to thank you for all the times you've been available, for your interesting and helpful discussions, and your questions, even though a bit challenging at times, they facilitated and promoted understanding.

Special thanks to Dr. Xiaona Li in the ICP-MS preparation and analysis, you're always eager to help, and I value your dedication and enthusiasm in teaching me to use different lab devices and methods. I am grateful to Dr. Stefanie Brachfeld for teaching me how to use the Labconco 4.5 Freezone freeze dryer device. I was amazed at how the samples looked like they were from another planet. Many thanks for teaching me complex subjects in an objective, motivating, and comprehensive style. I am deeply grateful to Brenda Godbolt and Dr. Jaime Grinberg at the Educational Foundations Department at Montclair State University for your patience, enthusiasm, and for always being supportive.

My Family and friends also deserve special thanks; Katica Pintado-Urbanc for all "cafesito times", they have been great breakthroughs all these years, many thanks for your patience and motivation. Oscar Olarte for our endless conversations and discussions, for sharing your passion in soils engineering and explaining complicated concepts in the simplest way possible. My Family for all their love, support, and tasty meals, especially my son Lukas who accompanied me unconditionally all this time Thanks!

Table of Contents

List of Figures

Tables

1 Introduction

The initial stage of the continental collision between India and Asia has complex consequences for the paleoenvironment and paleoclimate of the eastern Tethys ocean before its final closure (Aitchison et al., 2011; Hu et al., 2012; Jiang et al., 2016; Najman et al., 2010; Zhu et al., 2019). Numerous studies have investigated the age of the initial collision, but no consensus has been reached, with estimates ranging from ~65 to 34 million years ago (Ma) (Cai et al., 2011; Rowley, 1996; Searle et al., 1987; Singh, 2013; van Hinsbergen et al., 2012; Wang et al., 2012; Yin and Harrison, 2000). Furthermore, the growth of the Himalaya-Tibetan orogen is thought to have played a critical role in driving the long-term Cenozoic cooling through the negative silicate weathering feedback (Caves et al., 2016; Kump and Arthur, 1997; Raymo and Ruddiman, 1992). Despite these efforts, few studies have looked into the paleoenvironmental evolution of the eastern Tethys during the initial stage of the India-Asia continental collision (e.g., Kahsnitz, 2017; Wang et al., 2017; Zhang et al., 2012), possibly because of the sparse age constraint of this interval.

The Early Eocene Ypresian (ca. 56 to 47.8 Ma) is characterized by a hothouse climate with temperatures 15 ^{o}C warmer than the present day (Miller et al., 2020), and was punctuated by a series of rapid global warming events, known as Early Eocene hyperthermals (Nicolo et al., 2007; Slotnick et al., 2012). Large benthic foraminifera and negative carbon isotope excursion (CIE) allow for the recognition of the Paleocene-Eocene Thermal Maximum at Tingri in the Early Eocene Tethyan Himalaya (Zhang et al., 2013), but evidence for other Early Eocene hyperthermals is still lacking. Here, we present major and trace elements data and stable isotopes of carbon and nitrogen from the Qumiba section across the Early Eocene Enba and Zhaguo Formations in the hope to link the Early Eocene hyperthermal events to

geochemical characteristics of the siliciclastic sediments deposited in the foreland basin during the initial collision stage of the India-Asia continents.

2 Geological Background

Southern Tibet was located in the Tethyan Himalaya of the northern Greater Indian continental margin, formed by the collision of India and Asia in the Eocene epoch (~55 Ma) (Ding et al., 2016; Hu et al., 2016; Najman et al., 2017; Wang et al., 2008) (Figs 1 and 2). Prior to the collision, this region was part of the interior Tethys oceans in the Cretaceous. The collision of Indian-Asian plates resulted in the closure of the Neo-Tethys Ocean and subsequent stages of tectonic uplift and the formation of the Tibetan Plateau (Spicer et al., 2020; Wang et al., 2008). Therefore, the sediments of the Eocene period record the final stages of sedimentation on the southern margin of the Tethys ocean (Najman et al., 2010).

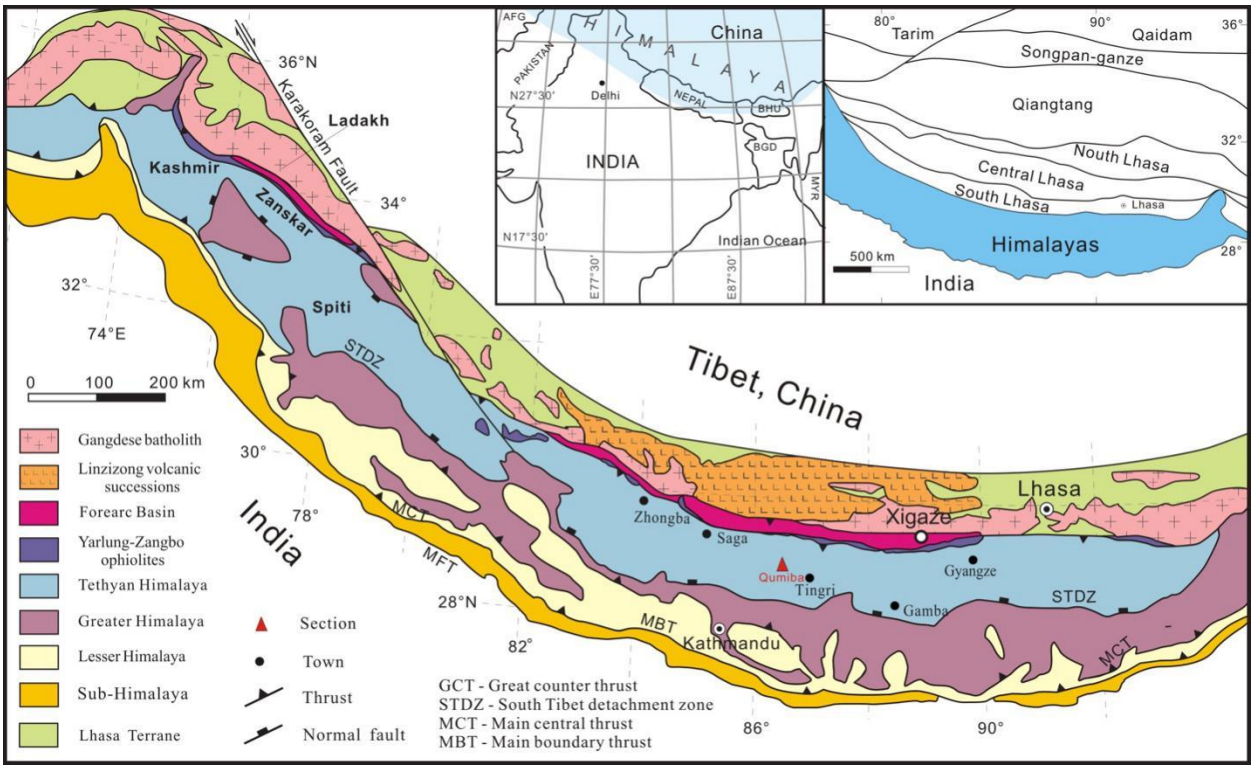

Figure 1. Geological map of the Himalayas modified from Hu et al. (2012) and Najman et al. (2017). The inset maps show the location of the Himalayas. The studied Qumiba section is shown in red triangle, which is located in the Tingri region in southern Tibet, China.

The study site, the Qumiba section, is located south of the Yarlung-Tsangpo structure in central Tethyan Himalayas in southern Tibet, west of the Zhepure Shan mountain in Tingri area (GPS N28º 41′ 26″, E86º 43′ 37″, elevation 4924 to 4970 m). Six stratigraphic units have been identified in the Zhepure Shan mountain (Willems et al., 1996), *i.e.* from oldest to youngest the Gamba Group (late Albian-early Santonian), the Zhepure Shanbei Formation (early Santonian-middle Maastrichtian), the Zhepure Shanpo Formation (middle Maastrichtian-early Paleocene), the Jidula Formation (Danian), the Zhepure Shan Formation (late Danian-Lutetian) and Zongpubei Formation (Lutetian or younger). The Gamba Group, Zhepure Shanbei Formation and Zhepure Shan Formation mainly consist of limestones and marls, while the Zhepure Shanpo Formation, Jidula Formation and Zongpubei Formation mainly consist of sandstones and mudstones. The Zongpubei Formation is composed of green-colored mudstones and sandstones overlain by red-colored mudstones, wackestones and sandstones, corresponding to Enba Fm. and Zhaguo Fm. respectively (Hu et al., 2012; Wang et al., 2002; Willems et al., 1996).

The studied successions consist of the upper part of Enba Formation and the lower part of the Zhaguo Formation (Najman et al., 2010). The Enba Formation consists of greenish-grey mudstones with thin interbedded sandstones and few thin limestones, with a thickness of approximately 105 m (Fig. 3). The quartzose sandstones are mature and lithic-rich, which are mainly volcanic fragments (Zhu et al., 2005). The sandstone beds become thicker and more abundant in the upper part of Enba Fm., with horizontal and wavy cross-lamination. Among them, hummocky cross-stratified beds can also be found, which implies the influence of storm waves (Figure 3; Zhu et al., 2005). It has been suggested that the Enba Fm. was deposited in an outer shelf environment, in which the mudstones were deposited by

suspension settling and sandstones by turbidity currents or high-energy events (Hu et al., 2012; Zhu et al., 2005).

The overlying Zhaguo Fm. (~75m) is composed of red mudstones and interbedded sandstones, and has similar lithologies to those of the Enba Fm. (Zhu et al., 2005). The boundary between Enba Fm. and Zhaguo Fm. is marked by a thick sandstone bed (~8m) featured by poorly sorted, angular, and pebble/cobble-sized grains derived from the underlying unit, interpreted as paleoregolith (Zhu et al., 2005). The subtle angular variations are observed by the minor dip differences between the Enba Fm. and the Zhaguo Fm. (≈11°). But it is still controversial whether unconformities and depositional hiatus exist at the Qumiba section (Najman et al., 2010; Hu et al., 2012). The thin sandstone beds in the Zhaguo Formation are commonly characterized by fining upwards, scoured bases, trough cross-lamination, horizontal lamination, and wavy cross-lamination. The sedimentary environment was interpreted as the shallow marine shelf environment (Wang et al., 2002).

The ages of the Enba Fm. and Zhaguo Fm. are Early Eocene, evidenced by no difference of the stratigraphically mixed calcareous nannofossil assemblages preserved in the two formations (Najman et al., 2010). Since the youngest assemblage can represent the age of the sediments, the ages of the two formations correspond to Ypresian stage (50.6–53.5 Ma) according to the nannofossil zones NP11–12, which is also consistent with the foraminiferal zones P7–8 (ca. 50.4–52.3 Ma) (Zhu et al., 2005; Najman et al., 2010).

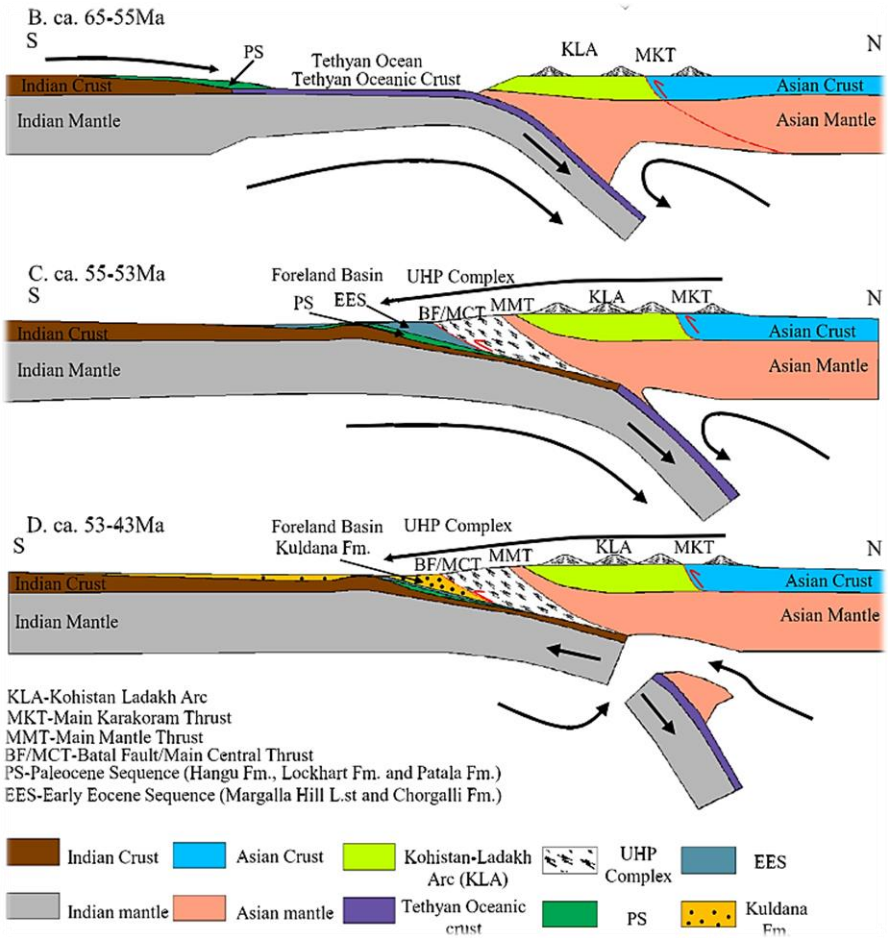

Figure 2. Tectonic evolution model of India–Asia collision (Ding et al., 2016)

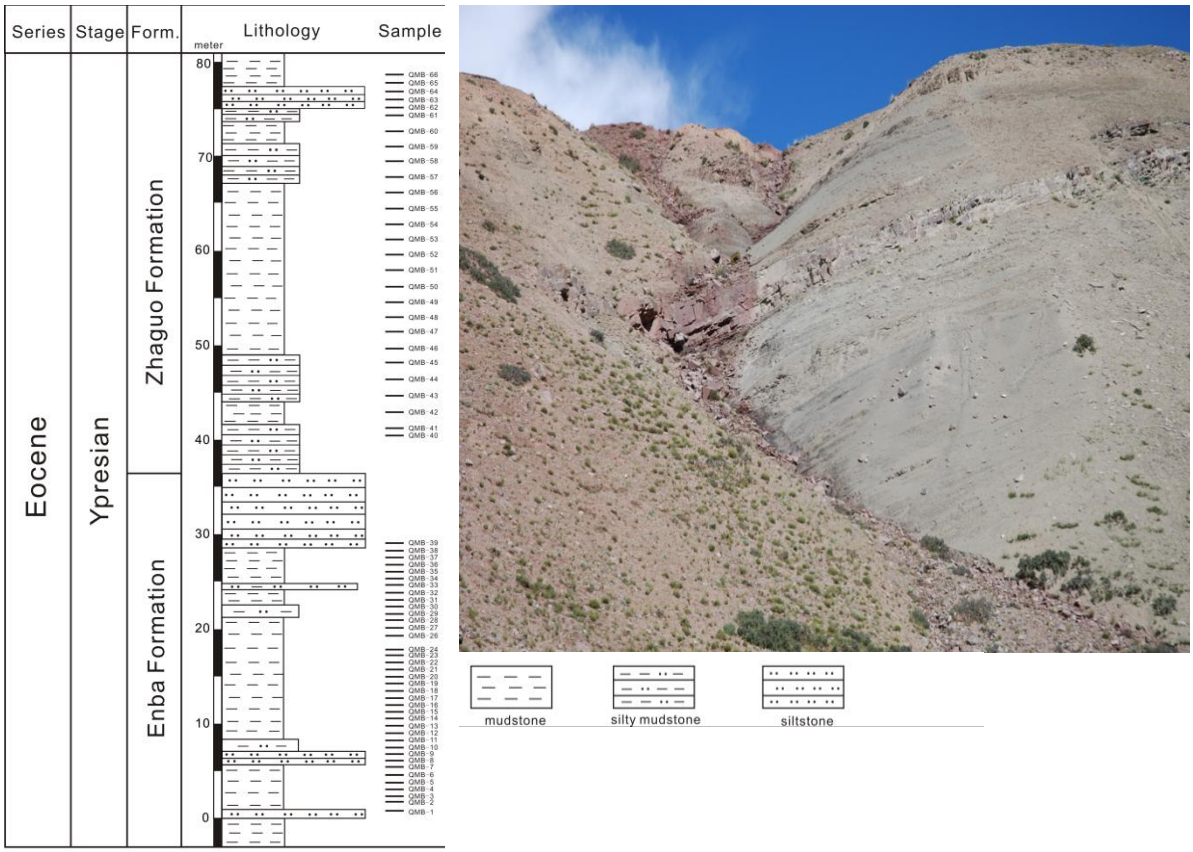

Figure 3. The stratigraphic log of the Eocene strata of the Qumiba section in this study, sample positions are shown as horizontal bars. Also shown is the field photography of the Qumiba section, which consists of Lower Eocene Enba and Zhaguo Formations with the thick sandstone as their boundary.

Motivation and Research Questions

Previous studies have shown that the nannofossil and foraminifera assemblages from the Lower Eocene Enba Formation and Zhaguo Formation are strongly influenced by the recycling and redeposition of Cretaceous and Paleocene age sediments from the Lhasa Terrain (Hu et al., 2012; Najman et al., 2010). This research aims to answer three research questions: 1) What are the paleoenvironmental and paleoclimatological responses in the eastern Tethyan ocean to tectonic forcings during India-Asia collision? 2) Are Early Eocene hyperthermal events recorded in the eastern Tethyan ocean? 3) What are the roles of recycled continental materials in the sediment provenance?

3 Materials and Methods

A total of 66 freshly excavated outcrop samples were collected from the sandstone and mudstone bearing the Qumiba section for this study, and each sample was taken one meter apart from the Enba Formation to the Zhaguo Formation (Table 1). These samples were examined for major, trace and rare earth elements (REE) analysis using an Inductively Coupled Plasma – Mass Spectrometry (ICP-MS) housed at the Department of Earth and Environmental Studies at Montclair State University. Thirty out of 66 samples were analyzed for stable carbon and nitrogen isotopes via EA-IRMS (Elemental Analyzer - Isotope Ratio Mass Spectrometer) in order to understand the carbon and nitrogen cycle of the Early Eocene in response to the closure of the Tethys Ocean and Himalaya uplift.

3.1 Major and Trace Element Analysis

All the Qumiba samples were crushed using a SPEX zirconia ceramics ball mill. Around 100 mg powder was mixed with 400 mg of ultrahigh-purity lithium metatetraborate flux ($^{(R)}$Spex-Certiprep) and fused in high-purity graphite crucibles at 1050 °C for 40 minutes in the Thermo Scientific™ Lindberg/Blue M^{TM} Box Furnace. Afterwards, molten samples were immediately dissolved in 50 ml of 7% HNO_3, then transferred for a second dilution of 6.5 mL of the sample plus HNO_3 (dilution factor of ~4000×) before ICP-MS analysis. The Milli-Q® Direct 8 Water Purification system was used for distilled and deionized experimental water; nitric acid from Fisher Scientific was of trace metal grade. Additional blanks and flux were prepared for analytical corrections to the analytical signal (<1.5% for all elements).

Instrument calibration was conducted using ten rock standards of the U.S. Geological Survey (USGS) (DNC-1, BHVO-2, G-2, W-2, BCR-2, GSP-2, QLO-1, AGV-2, BIR-1 and RGM-1). ICP-MS performed three analytical runs for all the samples, blanks and standards.

3.2 Stable carbon and nitrogen isotope analysis

Thirty samples were analyzed for stable carbon and nitrogen isotopes, and samples were first crushed using a SPEX zirconia ceramics ball mill. Powers are then dissolved in 10% HCl and neutralized with deionized distilled water and centrifuged. Solutions were decanted, and powders were dried using the Labconco 4.5 Freezone freeze dryer before folding in a tin boat and loaded in a Thermo Elemental Analyzer coupled to Delta V Advantage IRMS at Montclair State University (USA) to measure stable carbon and nitrogen isotopes. Precision is better than 0.5‰ for carbon, and better than 0.1‰ for nitrogen isotopes.

4 Results

Geochemical data for major, trace elements and REE concentrations, and stable carbon and nitrogen isotopes of the Qumiba section are shown in Table 1, 2, 3, 4 and 5. The major elements and trace elements are interpreted as weathering proxies and ocean redox proxies respectively. Trace elements and REE analysis are useful to reconstruct paleoenvironment and to trace sediment provenance. Based on the variations of major oxides contents, chemical weathering proxies, provenance proxies, redox proxies and nutrient proxies, the stratigraphic profile can be roughly divided into four parts (i.e. Part I: 0-10 m; Part II: 10-30 m; Part III: 40-66 m; Part IV: 66-80m) (Figure 4). In addition, Part II can be further subdivided to Part II-A (10-21m) and Part II-B (21-30m) because of the small variations inside.

4.1 Major element geochemistry

The major oxides are dominated by SiO_2 (61.2 – 77.0%), Al_2O_3 (10.3 – 19.8%), Fe_2O_3 (3.9 – 11.3%) and CaO (0.4 – 8.1%) (Figure 4**)**. Other major oxides such as MgO (1.5 – 3.5%), CaO (0.4 – 8.1%), K_2O (0.7 – 4.0%), MnO (0.0 – 0.5%), Na_2O (0.58 – 1.81%), TiO_2 (0.39 – 1.01%) and P_2O_5 (0.10 – 0.19%) exhibit small variations. The mudstone samples commonly show higher Al_2O_3 contents (12.3 – 19.8%, average 16.3%) and lower SiO_2 contents (61.2 – 73.2%, average 65.9%) than those of the sandstone samples (Al_2O_3: 11.5 – 12.7, average 10.3%; SiO_2: 69.4 – 77.0%, average 72.7%). Both mudstone and sandstone samples show a linear trend on the SiO_2 vs. Al_2O_3 (Figure 4), indicating they are similar to the siliciclastic rocks. Meanwhile, there is a strong positive correlation between Al_2O_3 and TiO_2 ($R^2 = 0.86$; *p*-value < 0.001), suggesting there is no significant difference in provenance between the mudstones and sandstones. The stratigraphic variations of major oxides contents of the Qumiba section along with the lithology is shown in Figure 4. The samples of Part I and Part IV display higher SiO_2 contents and lower Al_2O_3 contents than those of Part II and Part III. In addition, Part Ⅱ shows small variations inside, in which the samples of Part II-A have lower SiO_2 content and higher Al_2O_3 content than those of Part II-B.

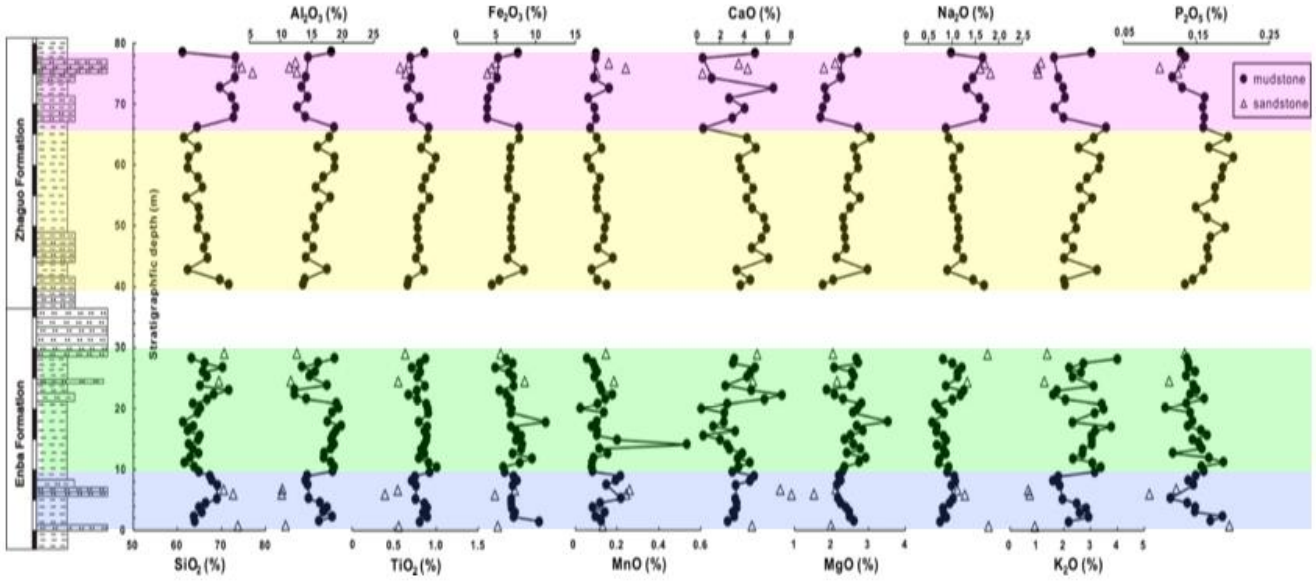

Figure 4. Content of major oxides from the Qumiba section, including SiO_2, Al_2O_3, TiO_2, Fe_2O_3, MnO, CaO, MgO, Na_2O, K_2O, and P_2O_5. Eight sandstone samples are plotted as triangles and 57 mudstone samples are plotted in closed circles.

4.2 Trace element geochemistry

Trace elements can be used to analyze the material provenance, water column redox and nutrient conditions through the concentrations, enrichment factors and the ratios of different trace elements. In order to interpret and compare the results properly, it is common to use enrichment factors (EF) of trace elements via aluminum (Al) normalization: $EF_{element\ X} = X/Al_{sample} / X/Al_{\ average\ shale}$ (Tribovillard et al., 2006). Europium anomaly (Eu/Eu*) (see below), Y/Ho, Th/Sc, Zr/Sc, La/Th vs. Hf, La-Th-Sc, Th/Co, and La/Sc can be used as sediment provenance proxies (Figure 11**;** discussed below) (Floyd and Leveridge, 1987; Gu et al., 2002). In addition, cerium anomaly (Ce/Ce*), U/Th ratios, and EF U, are paleoredox indices to help reconstruct the water column oxygen conditions at the study site (Figure 13). U/Th ratios range from 0.15 to 0.29 with an average of 0.17. EF U values range from 0.48 to 1.24 with an average of 0.71. The elements, such as phosphorus (P), barium (Ba), cobalt

(Co), and nickel (Ni), are used as the nutrient proxies to explore the paleoproductivity in the ocean (Anagnostou et al., 2011; Large et al., 2014; Tribovillard et al., 2006). The enrichment factors of the nutrient elements (P, Ba, Co and Ni) show the similar variation trends in the stratigraphic profile of the Qumiba section, in which the values of Part II-B and Part IV are relatively higher than those of other parts.

4.3 Rare earth elements geochemistry

Rare earth elements (REEs) tend to be constant in abundance and steady in properties due to their low mobilities and solubilities during sedimentary process (Cullers et al., 1988; McLennan et al., 1993; McLennan, 1989). Thus, the REE geochemistry can be used to trace the signature of the source materials of sedimentary rocks and speculate changes in tectonics and paleoenvironment (McLennan et al., 1993; McLennan, 1989). All the measured REE concentrations of both mudstone and sandstone samples are normalized to the North American shale composition (NASC) (Gromet et al., 1984). The shale normalized trace elements (X) are presented as X_{SN}. The traditional formula $Ce/Ce^* = Ce_{SN}/(0.5La_{SN}+ 0.5Pr_{SN})$ and $Eu/Eu^* = Eu_{SN}/(0.5Sm_{SN}+ 0.5Tb_{SN})$ was used to calculate the cerium (Ce) anomalies and europium (Eu) anomalies respectively (Bau and Dulski, 1996). Negative Ce/Ce* anomaly suggests low oxygen environment because Ce is depleted in oxic water due to its high redox sensitivity (German and Elderfield, 1990).

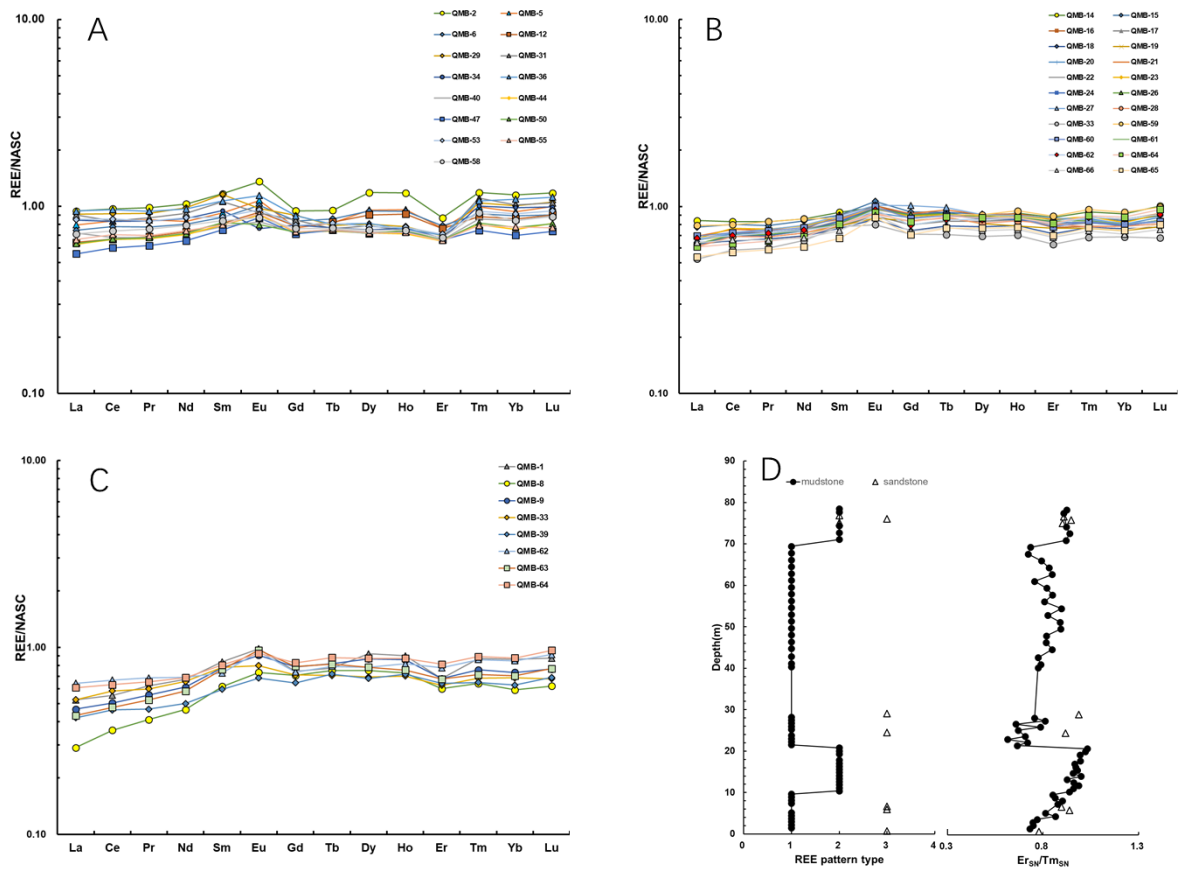

Figure 5. REE patterns of the samples in the Qumiba section. (A) Type 1 REE pattern; (B) Type 2 REE pattern; (C) Type 3 REE pattern; (D) The stratigraphic variations of the REE pattern types and Er_{SN}/Tm_{SN} ratios

The mudstone samples generally have higher total contents of REEs (ΣREE) (126.7 – 214.99 ppm, average 161.37 ppm) than those of sandstone samples (89.11 – 151.08 ppm, average 123.93 ppm). The NASC-normalized REE abundance patterns of sandstone and mudstone samples can be divided into three types, of which mudstone samples display as Type 1 and Type 2 and sandstone samples display as Type 3 (Figure 5). Type 1 and Type 2 mudstones exhibit similar trends with flat REE patterns, except that Type 1 mudstones yield lower Er_{SN}/Tm_{SN} ratios than those of Type 2 mudstones. Stratigraphically, the Type 1 mudstones mostly correspond to Part I, Part II-B and Part III, while Type 2 mudstones correspond to Part II-A and Part IV. The Type 3 sandstones exhibit a left-inclined REE

pattern with LREE (La, Ce, Pr, Nd, Pm, Sm, Eu, Gd) depleted. The Eu anomalies of all the samples show a small range of ratios from 0.87 to 1.31 with an average value of 1.14. The Eu/Eu* values decrease steadily from 1.3 to 0.87 in Part I and Part II from 0 to 30 m depth. Above 30 m, the Eu/Eu* values remain stable with an average of 1.2 in Part III and then increase to 1.3 in Part IV. The Ce anomalies show small fluctuations, ranging from 0.94 to 1.07 with an average value of 1.02. In general, the Ce/Ce* values of Part II-A and Part III are slightly higher than those of Part I, Part II-B and Part IV (Figure 6).

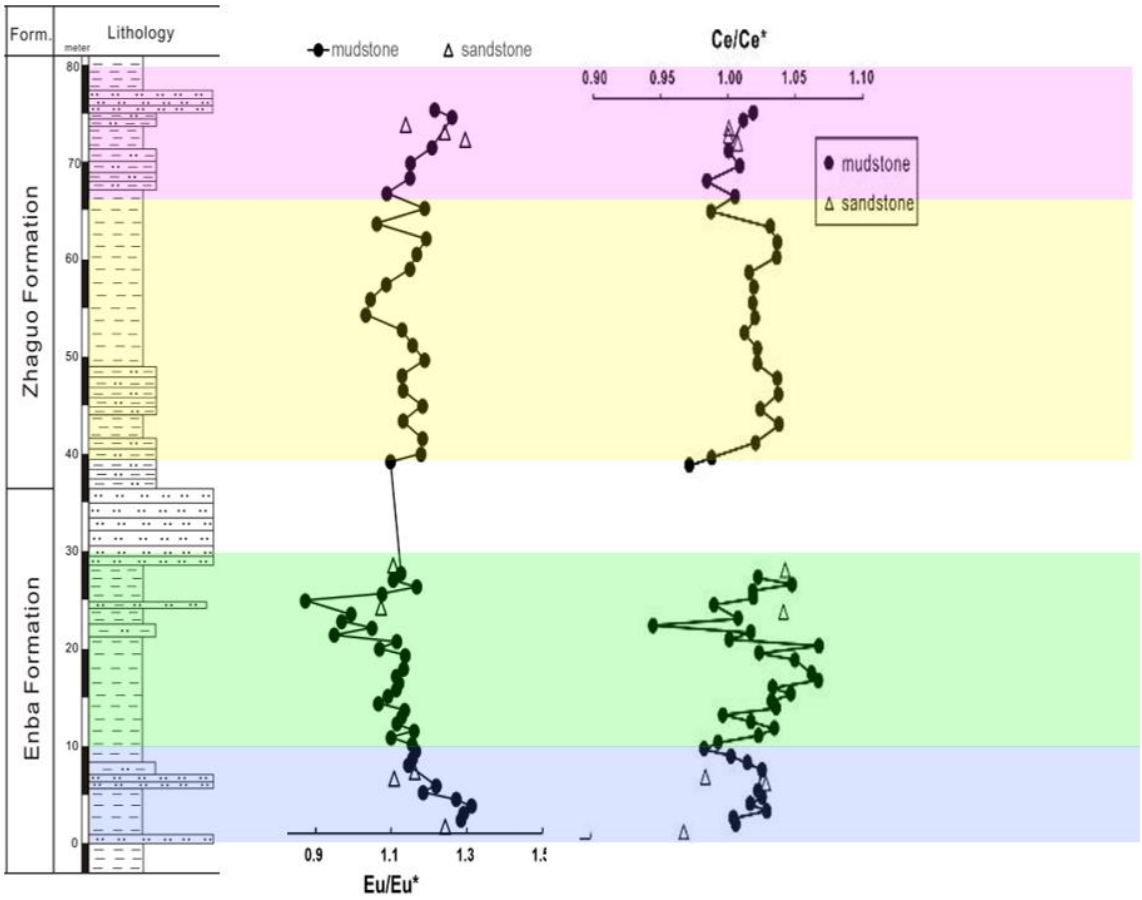

Figure 6. Eu/Eu* and Ce/Ce* anomalies cross-plot showing variations.

4.4 Stable carbon and nitrogen isotopes

The stable carbon ($\delta^{13}C$) and nitrogen isotopes ($\delta^{15}N$) are useful stratigraphic and paleoenvironmental tools. There are two stable isotopes of carbon in the Earth's crust, ^{13}C (1.11%) and ^{12}C (98.89%) (Tyson, 1995). Similarly, there are two stable isotopes of nitrogen, ^{15}N and ^{14}N respectively (Talbot, 2002). The relative abundance of the two carbon and nitrogen isotopes in a sedimentary sample can be expressed as $\delta^{13}C$ and $\delta^{15}N$ values in per mil (‰):

$$\delta^{13}C = [(^{13}C/^{12}C_{sample})/(^{13}C/^{12}C_{standard}) - 1] \times 1000 \qquad \text{(Eq. 1)}$$

$$\delta^{15}N = [(^{15}N/^{14}N_{sample})/(^{15}N/^{14}N_{standard}) - 1] \times 1000 \qquad \text{(Eq. 2)}$$

$\delta^{13}C$ and $\delta^{15}N$ can be used as indicators of marine productivity and water column redox conditions. Additionally, $\delta^{13}C$ gives information about carbon cycles and changes in the global climate. $\delta^{15}N$ variations indicate the intensity of denitrification, in which high intensity of denitrification suggests oceanic dysoxic condition. $\delta^{13}C_{org}$ and $\delta^{15}N_{org}$ values are plotted versus sample depth (Figure 7), and low values of $\delta^{13}C_{org}$ may be an indicator for Early Eocene hyperthermal 2 (ETM2 or H1; ca. 53.7 Ma). $\delta^{13}C_{org}$ values range from -25.4‰ to -33.8‰ with an average value of -29.2‰ and $\delta^{15}N_{org}$ values range from 4. 6‰ to 7.0‰ with an average of 5.6‰. The most abrupt decrease in $\delta^{13}C_{org}$ occurs at ~15m (-33.8‰), which is considered as a negative carbon isotope excursion (CIE), a possible sign of an Early Eocene hyperthermal (Figure 7).

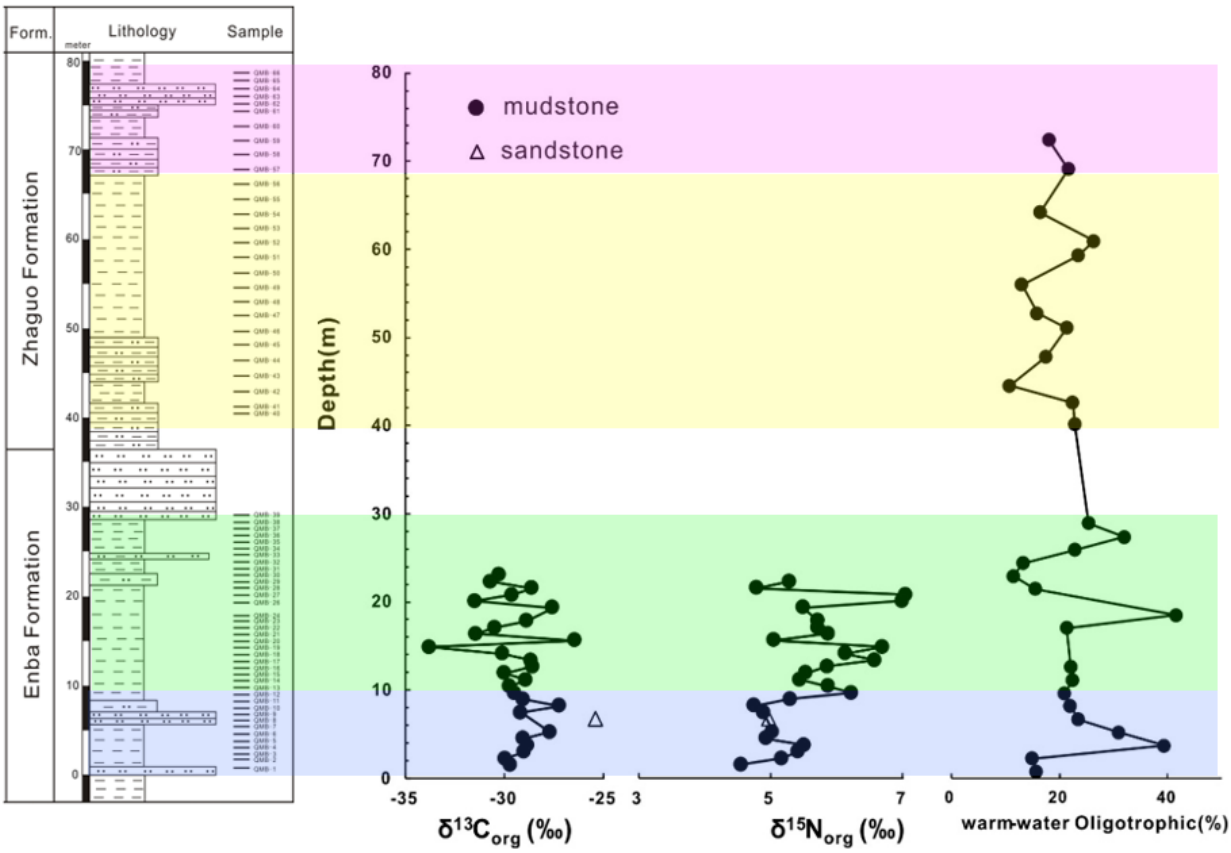

Figure 7. Stable carbon and nitrogen isotope profiles of the Enba Formation at the Qumiba section. Also shown is the warm-water oligotrophic Neochiastozygus calcareous nannofossils richness.

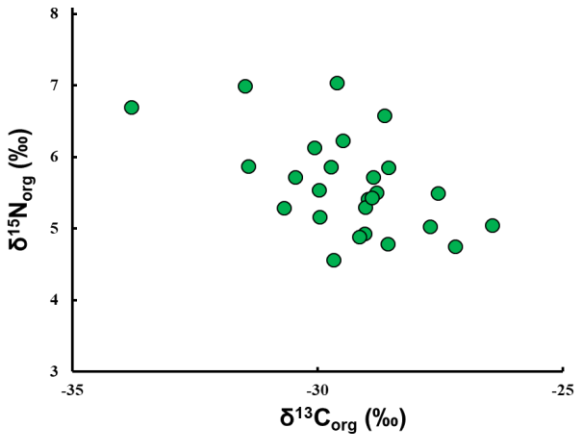

Figure 8. Cross-plot of $\delta^{13}C$ and $\delta^{15}N$ show statistically significant negative correlation (R^2 = 0.29, *p* value < 0.005), supporting warming ocean led to dysoxia condition.

In contrast, $\delta^{15}N_{org}$ values range from 4.8‰ to 7.0‰ and exhibit three pulses of enrichment at approximately 10 m, 15 m and 20 m in the Enba Formation (Figure 7). In general, $\delta^{15}N_{org}$ values exhibit an upward increasing trend. The highest $\delta^{15}N_{org}$ values correspond to the lowest $\delta^{13}C_{org}$, which is an indicator of increased ^{12}C input to the ocean-atmosphere system leading to warmer and more reduced water column conditions. The cross-plot of $\delta^{13}C_{org}$ and $\delta^{15}N_{org}$ from the Enba Formation shows a statistically significant negative correlation (Figure 8). $\delta^{13}C_{org}$ is influenced by primary productivity and $\delta^{15}N_{org}$ is affected by denitrification intensity through the reduction of nitrate by bacteria as a result of organic material input. Peaks of decreasing $\delta^{13}C_{org}$ and increasing $\delta^{15}N_{org}$ can suggest oversaturation of organic matter resulting in excessive nitrate causing restriction of oxygen transport related to dysoxic conditions.

5 Discussion

5.1 Provenance proxies

Several proxies have been suggested to infer the provenance of sedimentary rocks, including europium anomaly (Eu/Eu*), Y/Ho ratios, Th/Sc vs. Zr/Sc cross-plot, La/Th vs. Hf cross-plot (Floyd and Leveridge, 1987; Gu et al., 2002), La-Th-Sc and Th-Sc-Zr ternary diagrams (Bhatia and Crook, 1986) and Th/Co vs. La/Sc cross plot (Cullers, 2002). Here we take a multi-proxy approach to reconstruct the provenance of the sedimentary basin of the eastern Tethys.

The Qumiba section formed between 55 and 53 Ma in the Early Eocene in the subducting Paleo-Tethys foreland basin and was sourced mainly from the main mantle thrust (MMT), Kohistan-Ladakh, and main Karakoram thrust (MKT) according to Hu et al. (2012). The

La/Th vs. Hf cross-plot suggests these samples were derived from acidic arc source, with some influence of recycled sediment component (Figure 11), supporting the paleontological evidence of recycled Cretaceous and Paleocene fossils (Jiang et al., 2016). Both Th-Sc-Zr and La-Th-Sc ternary diagrams suggest the mudstone and sandstone samples from the Qumiba section are sourced from continental island arc (Figure 12), likely located in the Lhasa terrane as suggested by Hu et al. (2012).

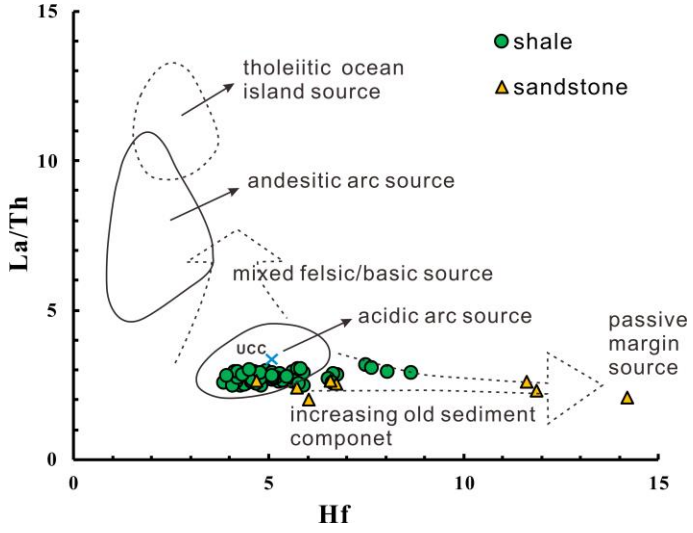

Figure 9. La/Th vs. Hf of both sandstone and mudstone samples modified from Floyd and Leveridge (1987).

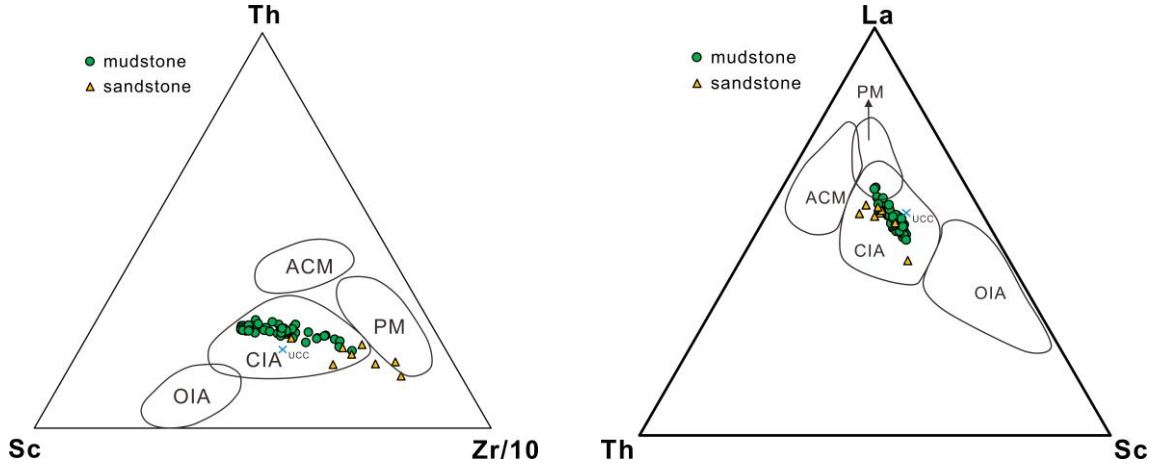

Figure 10. Th-Sc-Zr and La-Th-Sc ternary diagram showing tectonic discrimination (Bhatia and Crook, 1986); PM: passive margin; ACM: active continental margin; CIA: continental island arc; OIA: oceanic island arc.

5.2 Reconstructions of the Tethys ocean nutrient conditions

It has been suggested that marine surface productivity changes as a result of glacial-interglacial atmospheric CO_2 variations through the operation of biological pump (Berger et al., 1989; Paytan et al., 1996). The enrichment factor of phosphorus (P), barium (Ba), cobalt (Co), and nickel (Ni) have been suggested to be effective nutrient proxies (Anagnostou et al., 2011; Large et al., 2014; Tribovillard et al., 2006). For example, calibrations of deep-sea coral and sediments suggest that the enrichment of Ba element is a straightforward proxy for seawater dissolved Ba, which is an indicator of ocean paleoproductivity rate (Anagnostou et al., 2011; Dymond et al., 1992; Gingele et al., 1999). To interpret the elemental data as nutrient proxies, we follow Tribovillard et al. (2006) and calculate the enrichment factors (EF) of P, Ba, Co and Ni. $EF_{element\ X} = X/Al_{sample}/X/Al_{average\ shale}$, with values greater than 1 indicating element X is enriched compared to the average shale, and values less than 1 being depleted. We note that both EF_P and EF_{Ni} show strong enrichment at about 20 m (Part II), coincident with the maximum weathering indices, the lowest $\delta^{13}C_{org}$, and the maximum $\delta^{15}N_{org}$, consistent with warming-induced high weathering flux, causing high nutrient and low oxygen condition in the water column.

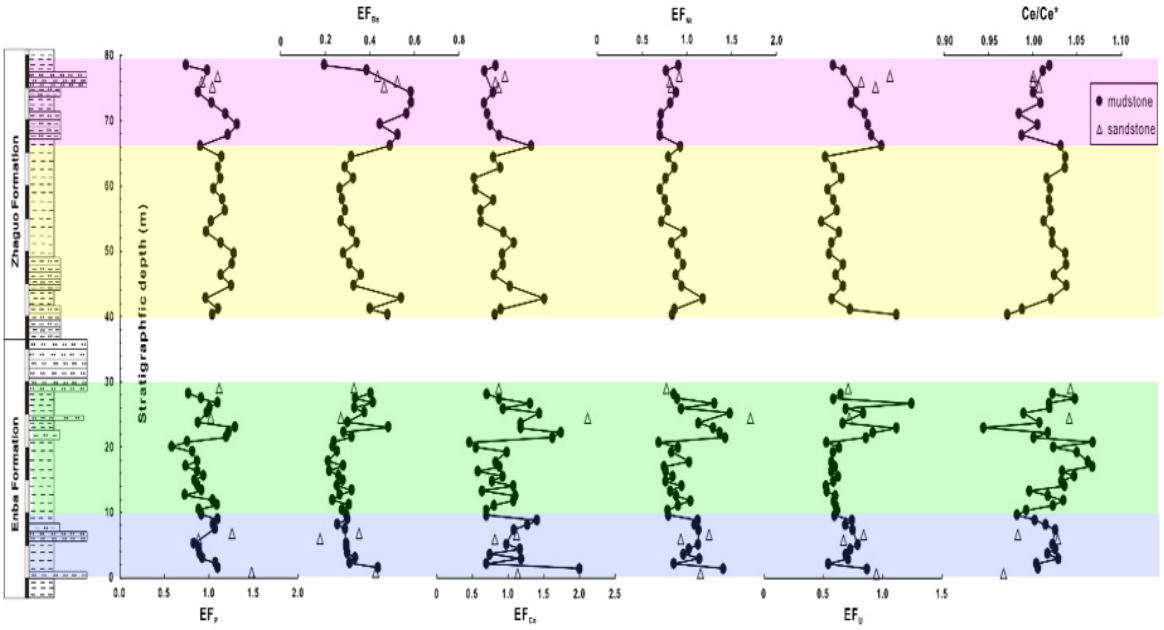

Figure 11. Enrichment factor of phosphorous, barium, cobalt, nickel and uranium and Ce anomalies from the Enba and Zhaguo Formation at the Qumiba section.

5.3 Reconstructions of the Tethys ocean redox conditions

Three trace element-based paleo-redox proxies are used in this study: Ce/Ce*, and EF_U (Figure 13) (Tribovillard et al., 2006). Ce/Ce* is a widely used paleoredox proxy for shallow water carbonates and mudstones (Murray et al., 1990; Webb and Kamber, 2000). The uranium (U) can always be precipitated by adsorption on or with organic matter in forms of +6 (i.e. UO_2^{2+}) in reducing environment, which high U contents indicate less oxic to anoxic conditions (Webb and Kamber, 2000; Tribovillard et al., 2006). The negative anomaly of Ce/Ce* and elevated EF_U both occur at ~20 m (top of Part IIA) and at ~66 m (top of Part III), consistent with increased chemical weathering driving low water column oxygen condition through elevated primary productivity (see nutrient proxies).

5.4 Chemical weathering intensity near the eastern Tethys

Chemical index of alteration (CIA) is a useful weathering proxy for mudstones generated in glaciated catchments (Nesbitt and Young, 1982; Wang et al., 2019), but controversies exist regarding its effectiveness in a wider range of global drainage basins (Li and Yang, 2010). Other chemical weathering proxies, such as chemical index of alteration without CaO (CIX) (Garzanti et al., 2014; Harnois, 1988), chemical index of weathering (CIW; Harnois, 1988), weathering index of Parker (WIP) (Parker, 1970), and weathering intensity scales (WIS) (Meunier et al., 2013) have also been proposed. Approaches that combine multiple weathering proxies are thought to be more reliable in fluvial drainage basins in China (Shao et al., 2012). We use three weathering proxies, namely CIA, CIX and WIP, to infer the weathering control on the composition of the siliciclastic sedimentary rocks in the Qumiba section.

$$CIA = Al_2O_3 / (Al_2O_3 + Na_2O + K_2O + CaO^*) \times 100 \quad \text{(Eq. 3)}$$

$$CIX = Al_2O_3 / (Al_2O_3 + Na_2O + K_2O) \times 100 \quad \text{(Eq. 4)}$$

$$WIP = (2Na_2O / 0.35 + MgO / 0.9 + 2K_2O / 0.25 + CaO^* / 0.7) \times 100 \quad \text{(Eq. 5)}$$

In order to calculate CIA and CaO*, the CaO incorporated in the silicate fraction needs to be known. An indirect method to quantify CaO* has been suggested by McLennan et al. (1993), and reasonable Ca/Na ratios of silicate should be assumed. The molar proportion of P_2O_5 needs to be subtracted from the molar proportion of total CaO. Then CaO* can be approximated by phosphate-CaO corrected values and Na_2O for samples with moles of CaO greater than Na_2O after phosphate-CaO correction (Fedo et al., 1995; McLennan et al., 1993; Yang et al., 2020). Because CIX does not require the knowledge of CaO*, we calculated CIX to compare the efficacy of this approach.

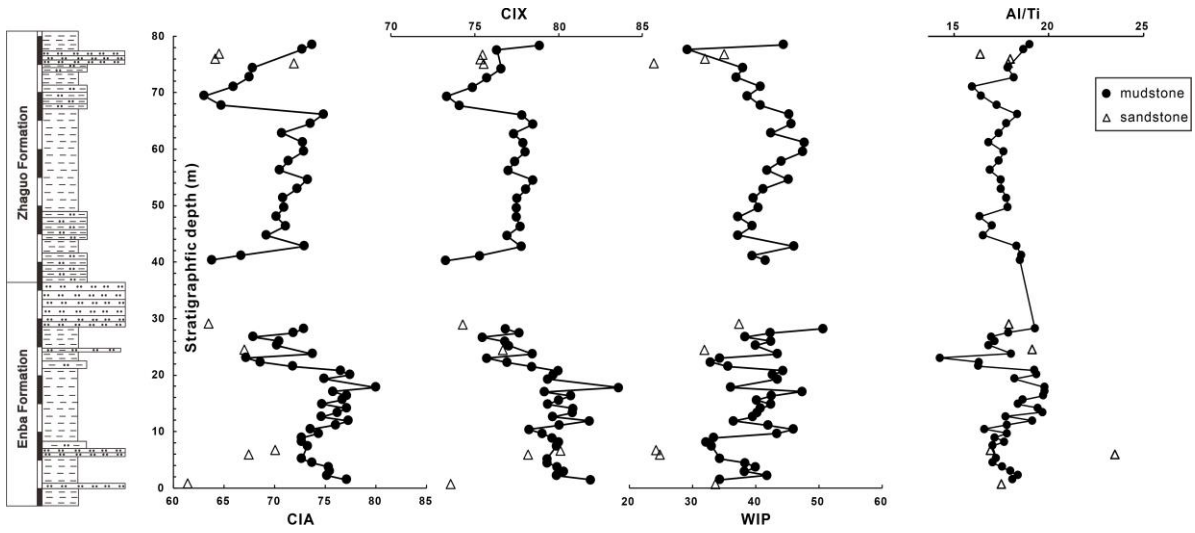

Figure 12. Calculated weathering proxies CIA, CIX and WIP for the mudstone samples from the Enba and Zhaguo Formation at the Qumiba section.

The major chemical weathering process in the continental upper crust is the formation of clay minerals through the degradation of feldspars, when Ca, Na and K ions are removed from the feldspars (Nesbitt and Young, 1982). In general, the CIA values for shales range around 70 to 75 due to the large amount of clay minerals, and the higher CIA indicates more intense chemical weathering (Bahlburg and Dobrzinski, 2011; Goldberg and Humayun, 2010). There appears to be three intervals where CIA, CIX and WIP show similar increasing trends: 10-20 m in the Enba Formation, ~40 m in the Zhaguo Formation, and 70-80 m in the Zhaguo Formation (Figure 9). These intervals also correspond to increased nutrient levels in the eastern Tethys ocean, as evidenced by the nutrient proxies shown below. The CIX vs. WIP cross-plot (Figure 10), shows the weathering trend of the mudstones from the four parts of the Qumiba section data plotted near the lowerleft corner suggest more sedimentary carbonate recycling.

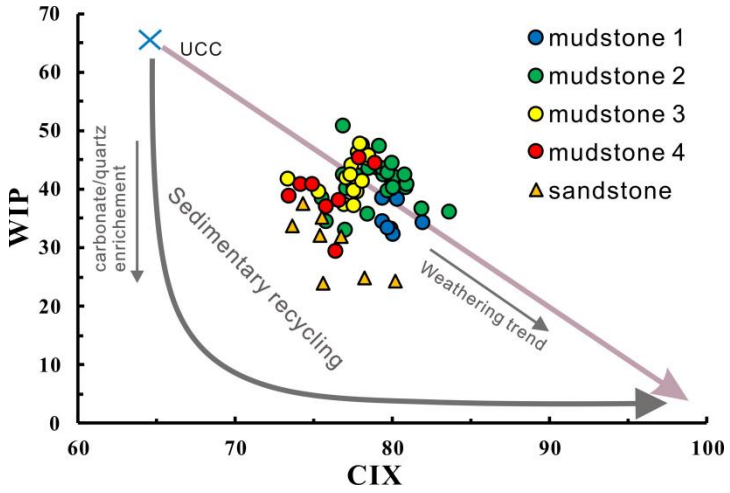

Figure 13. Weathering trend of the mudstones from the four parts of the Qumiba section (modified from Yang et al., 2020).

5.5 Carbon and nitrogen cycle during the Early Eocene Tethys

During carbon assimilation, marine phytoplankton preferentially take up ^{12}C due to the kinetic effect (Galimov, 1985). Marine organic matter is composed of both marine and terrigenous particulate organic sources (Andrews et al., 1998; Dean et al., 1986). Studies have shown that modern terrestrial organic matter exhibits lower $\delta^{13}C$ values (average -27‰; Diefendorf et al., 2010) than marine organic matter (-22‰; Hayes et al., 1999) as shown in the Global distribution of modern $\delta^{13}C$ value ranges in carbon dioxide, methane, dissolved inorganic and organic carbon (DIC, DOC), particulate organic matter (OM) and carbonates (Figure 14). In the Cretaceous, however, marine organic matter is shown to have much lower values (average -28‰) (Arthur et al., 1985), likely because the CO_2 levels were much higher than the present day. The variation of marine $\delta^{13}C_{org}$ is often interpreted as the relative proportions of marine versus terrestrial sources of the sedimentary organic matter (Hedges

and Parker, 1976; Sackett, 1964). They can also be used as global stratigraphic correlation tools (chemostratigraphy) and paleoenvironmental tools (Ando et al., 2002; Erbacher et al., 2005; Mackensen and Schmiedl, 2019; Popp et al., 1997; Ruhl et al., 2009).

The Early Eocene eastern Tethys receives two primary sources: recycled organic matter from continental weathering and marine organic matter. The $\delta^{15}N_{org}$ values ranging from -5‰ to 18‰ indicate terrigenous organic input (Peters et al., 1978; Schoeninger and DeNiro, 1984). The 4.6 to 7.0‰ $\delta^{15}N_{org}$ values in the Qumiba samples suggest terrigenous organic matter influence. Additionally, the negative correlation between $\delta^{13}C_{org}$ and $\delta^{15}N_{org}$ suggest increasing influence of nitrate reduction (Jacot Des Combes et al., 2008). To understand the relative contribution of recycled organic matter and marine organic matter, a simple two end-member mixing equation can be used, in which we assign mean $\delta^{13}C$ values to recycled Cretaceous and Paleogene organic matter ($\delta^{13}C_{recycled}$) and coeval marine organic matter ($\delta^{13}C_{MOM}$):

$$F_{recycled}\ (\%) = (\delta^{13}C_{org} - \delta^{13}C_{MOM})/(\delta^{13}C_{recycled} - \delta^{13}C_{MOM}) \times 100 \qquad \text{(Eq. 6)}$$

$\delta^{13}C_{org}$ is the measured carbon isotope value from the Qumiba section, $\delta^{13}C_{MOM}$ is the carbon isotope value of coeval marine organic matter, $\delta^{13}C_{recycled}$ is the recycled Cretaceous and Paleogene marine organic matter.

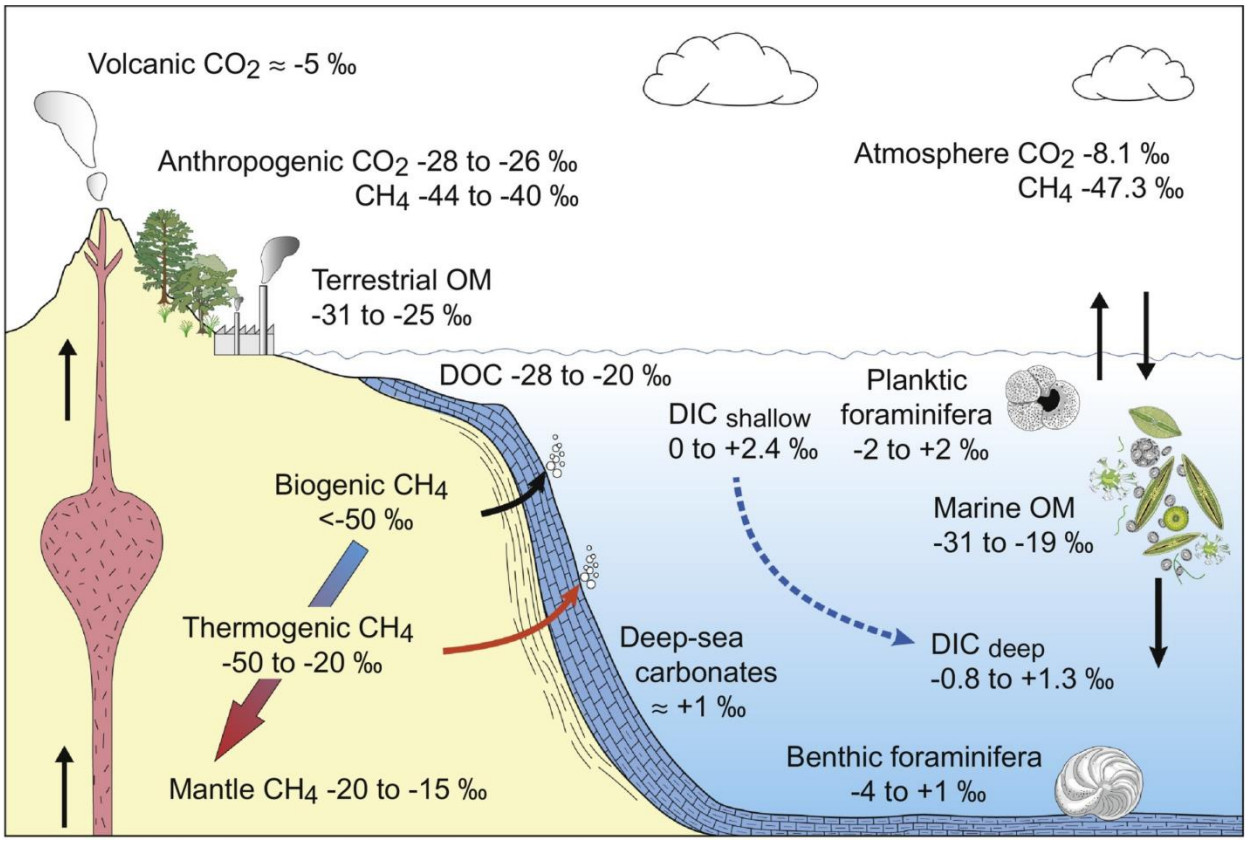

Figure 14. Global distribution of modern $\delta^{13}C$ value ranges in carbon dioxide, methane, dissolved inorganic and organic carbon (DIC, DOC), particulate organic matter (OM) and carbonates based on Mackensen and Schmiedl (2019).

Compared to marine $\delta^{13}C$, nitrogen isotopes are used less frequently as stratigraphic correlation tool, but widely used as paleoenvironmental proxies (Altabet, 2006; Kashiyama et al., 2008; Rau et al., 1987; Sigman et al., 2009). Similar to carbon isotope fractionation, primary producers preferentially use ^{14}N relative to ^{15}N in nitrate during nitrate assimilation because of kinetic effects (Montoya, 1994; Waser et al., 1998). The degree of nitrogen fractionation depends on the amount of available nitrate and the rate of nitrate consumption (Deutsch et al., 2004; Sigman and Haug, 2003). The largest nitrogen fractionation incurs during denitrification (the microbial process of nitrate reduction and the ultimate production of N_2) (Dähnke and Thamdrup, 2013; Kritee et al., 2012) as showing in the Global marine nitrogen cycle (Figure 15). Foraminifera bound nitrogen isotopes show that the early

Cenozoic is characterized by elevated $\delta^{15}N$ values, an indicator of intensified denitrification facilitated by reduced oxygen concentration (Kast et al., 2019). Elevated $\delta^{15}N$ values at the lower Enba Formation reflect stronger denitrification in the Qumiba section, supporting an episodic water column oxygen reduction.

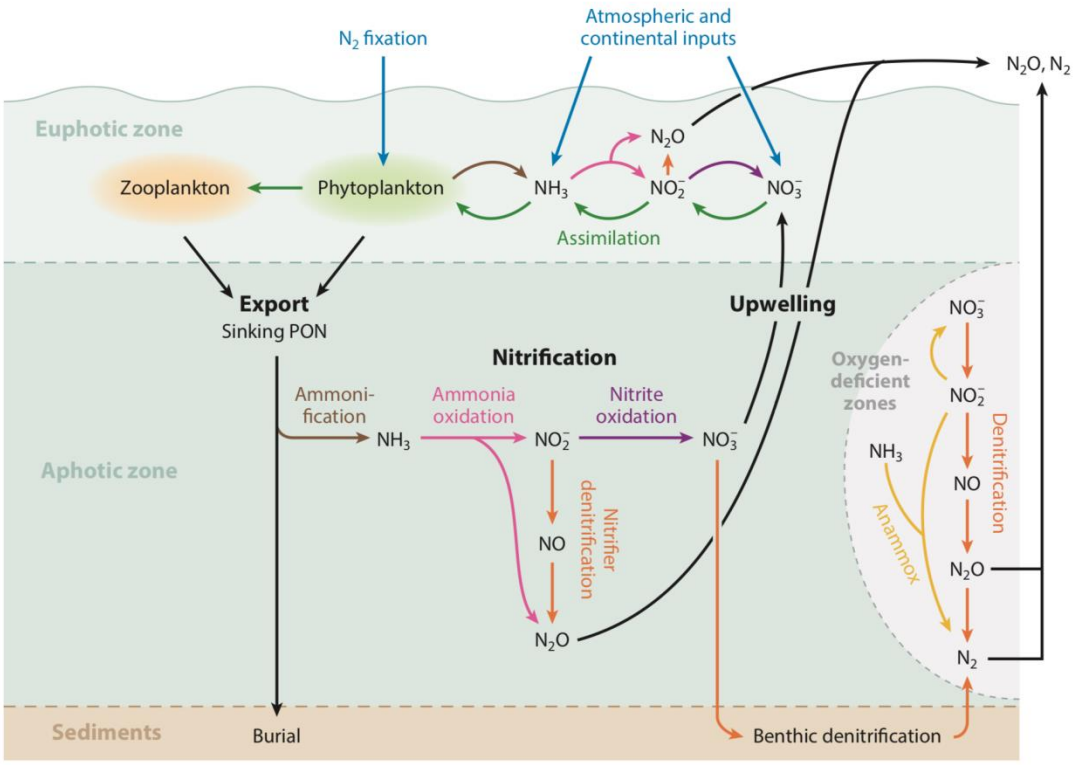

Figure 15. Global marine nitrogen cycle based on Casciotti et al. (2016).

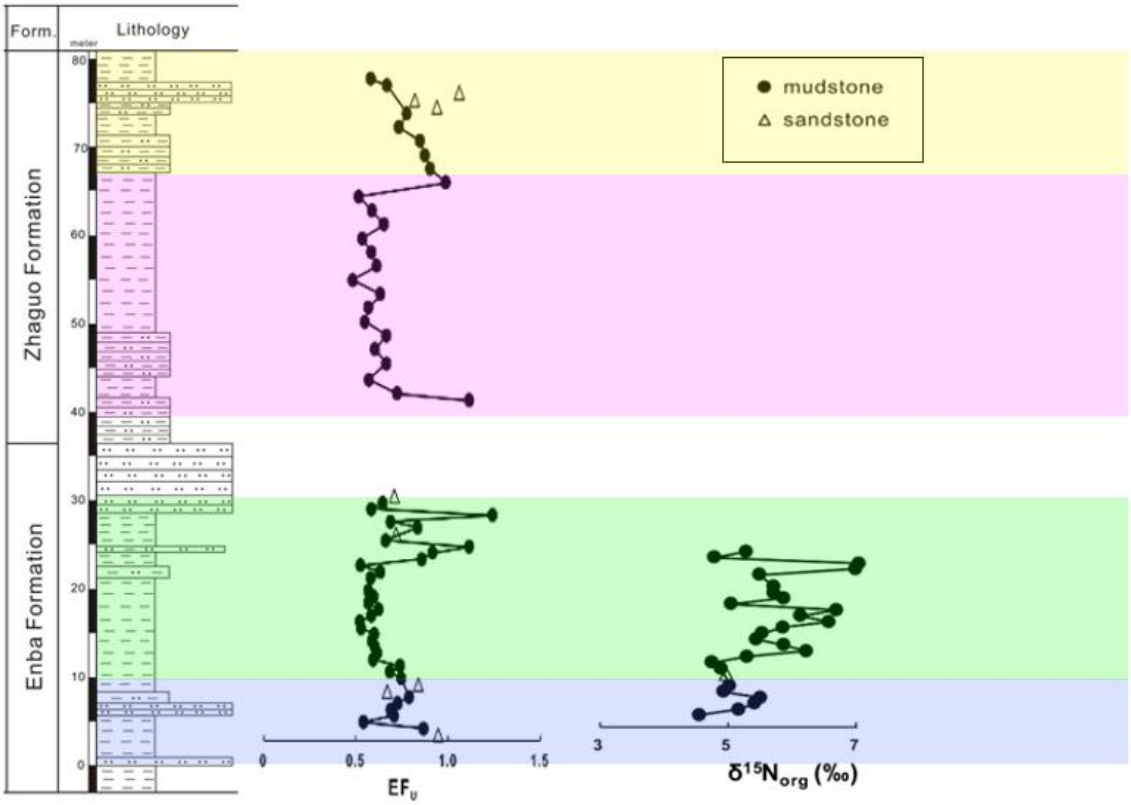

Figure 16. EF_U, and $\delta^{15}N_{org}$ showing low oxygen, and denitrification for upper part of ~0 - 30m section.

6 Conclusion

The initial stage of the India-Asia collision occurred during the early Cenozoic ice-free greenhouse world, which was punctuated by a series of transient global warming events, likely driven by volcanic eruptions and orbital forcings. To understand the paleoenvironmental conditions of the Early Eocene eastern Tethys ocean before its final closure, we study the youngest marine successions from the southern Tibet in their geochemical characteristics. We report new major, trace element geochemistry and stable carbon and nitrogen isotope data of the Early Eocene strata deposited in a shallow marine foreland basin prior to the main stage of India-Asian continent collision at Qumiba section in the Tingri County, southern Tibet. Major element geochemistry and weathering indices suggest that the Eocene southeastern Tethys may have experienced episodic input of nutrient-rich weathering supplies and the development of hypoxia in the water column, consistent with the warm and humid climate in the Early Eocene (Figure 16).

Table 1. Whole-rock compostions of the Qumiba section in the Tingri County, southern Tibet

Depth (m)	Sample	SiO2	TiO2	Al2O3	Fe2O3	MnO	MgO	CaO	Na2O	K2O	P2O5	Total
0.74	QMB-1	73.69	0.56	10.86	5.23	0.13	1.98	4.72	1.77	0.91	0.15	100.00
1.49	QMB-2	64.00	0.81	16.23	10.45	0.12	2.61	2.70	0.75	2.17	0.17	100.00
2.23	QMB-3	63.73	0.90	18.32	7.24	0.10	2.48	3.24	0.88	2.92	0.19	100.00
2.97	QMB-4	65.53	0.85	16.93	7.40	0.14	2.47	3.12	0.83	2.58	0.15	100.00
3.71	QMB-5	64.86	0.90	17.55	6.97	0.08	2.39	3.45	0.82	2.83	0.15	100.00
4.46	QMB-6	66.42	0.86	16.38	6.93	0.12	2.25	3.46	0.96	2.49	0.14	100.00
5.20	QMB-7	68.95	0.76	14.56	6.90	0.22	2.17	3.35	1.02	1.96	0.11	100.00
5.94	QMB-8	72.62	0.39	10.25	4.82	0.24	1.52	8.09	1.27	0.71	0.09	100.00
6.68	QMB-9	70.46	0.54	10.25	7.35	0.26	2.10	7.13	1.11	0.66	0.12	100.00
7.43	QMB-10	69.05	0.76	14.43	7.10	0.15	2.14	3.38	0.99	1.85	0.15	100.00
8.17	QMB-11	67.79	0.71	14.01	7.65	0.20	2.25	4.58	1.07	1.60	0.14	100.00
8.91	QMB-12	67.35	0.75	14.35	7.21	0.22	2.19	4.94	1.05	1.80	0.15	100.00
9.65	QMB-13	64.89	0.93	18.41	6.08	0.08	2.30	3.10	0.90	3.15	0.16	100.00
10.40	QMB-14	63.87	1.01	18.68	5.92	0.08	2.35	3.61	0.93	3.38	0.16	100.00
11.14	QMB-15	61.59	0.91	18.12	7.99	0.08	2.74	4.58	0.73	3.07	0.19	100.00
11.88	QMB-16	62.91	0.80	16.94	9.58	0.09	2.92	3.51	0.74	2.34	0.17	100.00
12.62	QMB-17	64.85	0.86	17.04	7.08	0.16	2.42	3.91	0.88	2.69	0.12	100.00
13.37	QMB-18	63.49	0.83	18.09	8.17	0.11	2.78	2.84	0.82	2.71	0.16	100.00
14.11	QMB-19	62.57	0.86	18.64	8.28	0.54	2.59	2.65	0.68	3.04	0.15	100.00
14.85	QMB-20	64.68	0.89	18.22	7.53	0.20	2.35	2.06	0.88	3.04	0.15	100.00
15.60	QMB-21	65.14	0.89	18.54	8.18	0.10	2.52	0.61	0.82	3.03	0.16	100.00
16.34	QMB-22	62.35	0.87	18.99	7.53	0.11	2.85	3.31	0.67	3.16	0.16	100.00
17.08	QMB-23	63.60	0.90	19.79	6.90	0.08	2.68	1.46	0.69	3.77	0.14	100.00
17.82	QMB-24	61.31	0.80	17.60	11.27	0.10	3.52	2.36	0.58	2.32	0.15	100.00
19.31	QMB-26	64.57	0.91	18.38	6.90	0.14	2.58	2.39	0.84	3.15	0.14	100.00
20.05	QMB-27	65.24	0.90	19.42	6.97	0.03	2.71	0.44	0.72	3.48	0.11	100.00
20.79	QMB-28	63.57	0.89	19.05	6.72	0.11	2.81	2.64	0.66	3.41	0.14	100.00
21.54	QMB-29	66.70	0.78	14.18	6.82	0.14	2.31	5.82	1.02	2.07	0.16	100.00
22.28	QMB-30	68.27	0.68	12.26	6.34	0.18	2.07	7.29	1.18	1.59	0.14	100.00
23.02	QMB-31	71.63	0.78	12.30	5.46	0.13	1.87	4.69	1.25	1.74	0.15	100.00
23.76	QMB-32	65.09	0.87	17.52	7.22	0.12	2.53	2.51	0.87	3.12	0.15	100.00
24.51	QMB-33	69.37	0.55	11.65	8.60	0.19	2.14	4.81	1.33	1.26	0.11	100.00
25.25	QMB-34	66.77	0.78	14.68	7.17	0.09	2.61	4.31	1.13	2.33	0.14	100.00
25.99	QMB-35	65.76	0.82	15.58	6.64	0.11	2.56	4.62	1.12	2.64	0.15	100.00
26.74	QMB-36	70.21	0.71	13.45	4.91	0.10	2.06	5.02	1.21	2.20	0.14	100.00
27.48	QMB-37	66.22	0.81	16.05	7.10	0.09	2.72	3.14	1.01	2.72	0.14	100.00
28.22	QMB-38	63.15	0.87	18.76	6.27	0.06	2.67	3.27	0.81	4.00	0.14	100.00
29.04	QMB-39	70.62	0.63	12.62	5.54	0.15	2.03	5.16	1.75	1.37	0.13	100.00
40.33	QMB-40	71.67	0.66	13.67	4.48	0.15	1.75	3.75	1.69	2.04	0.13	100.00
41.16	QMB-41	69.63	0.67	13.91	5.44	0.11	2.04	4.59	1.45	2.01	0.15	100.00
42.80	QMB-42	62.32	0.86	17.48	8.55	0.08	2.97	3.45	0.91	3.24	0.16	100.00
44.74	QMB-43	66.79	0.76	14.06	6.47	0.18	2.13	6.19	1.24	2.01	0.17	100.00
46.39	QMB-44	65.98	0.81	15.31	7.03	0.11	2.38	4.73	1.11	2.37	0.16	100.00
48.03	QMB-45	66.67	0.78	14.17	6.93	0.14	2.36	5.59	1.16	2.04	0.17	100.00
49.68	QMB-46	64.54	0.78	15.60	6.86	0.14	2.33	5.96	1.13	2.46	0.19	100.00
51.33	QMB-47	65.04	0.77	15.32	6.93	0.15	2.31	5.78	1.13	2.38	0.17	100.00
52.97	QMB-48	64.76	0.83	16.21	6.99	0.11	2.50	4.77	1.02	2.66	0.15	100.00
54.62	QMB-49	62.02	0.93	18.06	7.59	0.10	2.77	4.29	1.00	3.06	0.18	100.00
56.26	QMB-50	65.61	0.83	15.67	6.60	0.10	2.42	4.86	1.14	2.58	0.18	100.00
57.91	QMB-51	64.73	0.88	16.93	.49	0.12	2.45	4.23	1.12	2.87	0.19	100.00
59.55	QMB-52	62.35	0.95	18.75	6.83	0.08	2.71	3.80	1.04	3.31	0.19	100.00
61.19	QMB-53	62.51	1.00	18.73	6.79	0.06	2.68	3.65	1.02	3.36	0.20	100.00
62.84	QMB-54	64.67	0.83	16.01	6.79	0.13	2.61	5.07	1.17	2.55	0.17	100.00
64.49	QMB-55	61.51	0.90	17.88	7.97	0.10	3.06	4.34	0.93	3.11	0.19	100.00
66.14	QMB-56	64.53	0.91	18.66	7.90	0.07	2.72	0.59	0.88	3.58	0.16	100.00
67.78	QMB-57	72.69	0.73	14.00	3.88	0.10	1.69	3.09	1.67	1.99	0.16	100.00
69.43	QMB-58	73.19	0.69	12.72	3.90	0.09	1.76	4.12	1.72	1.66	0.16	100.00
71.07	QMB-59	72.30	0.81	14.37	3.98	0.06	1.87	2.82	1.58	2.05	0.16	100.00
72.72	QMB-60	69.65	0.66	13.42	4.31	0.16	1.82	6.56	1.32	1.97	0.13	100.00
74.36	QMB-61	73.05	0.71	14.09	5.12	0.09	2.25	1.35	1.44	1.79	0.12	100.00
75.19	QMB-62	76.96	0.64	12.68	3.91	0.10	2.22	0.52	1.81	1.04	0.13	100.00
76.01	QMB-63	74.50	0.57	11.42	4.40	0.24	1.78	4.38	1.61	1.00	0.10	100.00
76.83	QMB-64	73.11	0.68	12.40	4.96	0.16	2.10	3.62	1.70	1.15	0.13	100.00
77.65	QMB-65	73.18	0.70	14.50	5.26	0.10	2.27	0.57	1.66	1.63	0.14	100.00
78.48	QMB-66	61.20	0.86	18.23	7.75	0.10	2.70	5.02	0.98	3.02	0.13	100.00

*Major elements expressed in weight percent % (wt. %)

Table 2. Trace elements of the Qumiba section

Depth (m)	Sample	Sc	V	Cr	Co	Ni	Ga	Rb	Sr	Y	Zr	Nb	Cs	Ba	Hf	Ta	Pb	Th	U
0.74	QMB-1	10.20	66.03	117.81	13.89	50.67	15.78	42.00	119.36	27.87	262.78	11.65	2.24	180.69	6.74	0.81	21.27	9.22	1.83
1.49	QMB-2	23.53	182.25	129.03	36.62	92.51	20.26	119.19	195.65	36.54	205.80	20.68	7.54	275.91	5.63	1.39	35.31	14.47	2.51
2.23	QMB-3	19.25	139.98	99.81	14.39	63.31	18.50	114.02	163.05	25.10	153.60	15.90	6.79	223.53	4.32	1.09	26.77	12.03	1.77
2.97	QMB-4	22.66	160.61	120.63	22.57	78.20	19.63	128.59	188.23	29.02	186.67	18.42	7.82	221.84	5.17	1.32	37.18	13.51	2.14
3.71	QMB-5	23.05	155.43	115.76	14.76	68.58	19.29	135.50	184.99	29.38	190.59	18.93	8.32	208.87	5.26	1.28	43.72	13.65	2.16
4.46	QMB-6	19.22	136.09	112.14	21.60	68.02	18.58	110.66	177.54	29.32	198.81	16.28	6.70	193.73	5.63	1.10	36.12	12.80	2.12
5.20	QMB-7	15.38	117.03	104.68	16.01	66.45	17.99	89.24	174.15	28.58	197.95	15.05	5.28	169.25	5.58	1.07	13.27	11.84	2.05
5.94	QMB-8	10.76	57.07	80.16	9.42	38.68	14.42	28.40	201.34	23.14	232.31	9.46	1.75	72.01	6.02	0.48	20.29	6.51	1.22
6.68	QMB-9	9.05	70.47	113.23	12.93	51.88	15.14	27.58	197.01	26.57	256.46	9.84	1.81	142.88	6.59	0.66	26.69	7.92	1.53
7.43	QMB-10	15.35	126.72	111.62	17.58	66.29	17.70	83.50	168.30	27.93	201.40	15.25	5.18	164.84	5.45	0.99	34.23	11.38	1.92
8.17	QMB-11	13.89	105.12	117.85	20.09	61.79	16.58	69.39	165.88	26.63	228.40	12.00	4.32	141.68	5.91	0.83	51.42	10.04	1.71
8.91	QMB-12	15.10	112.95	104.26	22.78	65.29	17.45	79.49	215.01	28.25	199.51	13.83	4.78	172.82	5.36	0.93	54.81	10.89	1.90
9.65	QMB-13	19.16	153.32	101.12	14.41	59.30	19.35	133.25	169.82	26.44	169.00	16.56	8.50	215.08	4.64	1.06	36.11	12.39	1.95
10.40	QMB-14	20.09	151.43	107.41	14.67	59.60	19.21	142.68	174.33	27.93	177.40	17.45	8.96	199.73	4.94	1.14	51.76	12.62	2.06
11.14	QMB-15	18.91	155.06	99.94	16.45	66.41	19.31	136.10	170.05	27.51	162.82	16.81	8.87	215.72	4.50	1.10	42.99	11.65	1.95
11.88	QMB-16	15.50	134.90	90.29	20.56	71.40	18.20	99.48	143.41	25.01	146.24	13.92	6.49	152.99	4.13	0.93	36.37	10.20	1.78
12.62	QMB-17	16.58	127.51	97.49	21.19	60.78	18.35	114.43	162.09	25.72	173.07	15.36	7.39	177.34	4.80	1.02	104.80	11.44	1.83
13.37	QMB-18	15.79	137.18	88.83	12.92	59.95	18.48	113.35	133.10	23.95	145.67	13.70	7.32	223.19	4.13	0.93	57.46	11.40	1.70
14.11	QMB-19	16.93	142.78	95.68	22.60	71.06	19.00	122.14	128.16	23.86	144.10	13.97	7.80	183.90	3.93	0.89	28.57	10.80	1.73
14.85	QMB-20	18.07	138.24	96.99	15.93	56.32	19.11	129.86	131.76	25.09	159.94	15.32	8.26	199.34	4.43	1.00	82.79	11.64	1.90
15.60	QMB-21	18.06	146.59	98.73	19.30	63.12	19.07	124.62	110.95	26.36	164.67	15.56	8.11	187.28	4.54	1.04	69.45	11.40	2.06
16.34	QMB-22	18.09	146.65	99.49	12.34	58.82	19.37	133.03	130.86	24.86	142.90	14.61	8.77	164.18	3.90	0.94	30.72	10.58	1.92
17.08	QMB-23	19.68	153.10	101.01	19.66	59.79	19.81	158.49	120.20	26.23	154.03	15.42	10.07	220.39	4.29	1.01	53.73	12.22	2.11
17.82	QMB-24	18.05	128.73	92.64	16.34	73.18	18.39	102.43	124.59	25.61	140.49	14.15	6.58	147.77	3.85	0.90	57.22	10.87	1.79
19.31	QMB-26	17.21	133.42	98.67	20.34	61.69	18.95	128.17	131.97	25.63	152.38	15.13	8.11	181.11	4.38	0.97	66.73	11.22	1.91
20.05	QMB-27	17.81	155.53	103.74	12.00	71.15	19.43	146.73	113.74	26.74	152.44	15.57	9.66	179.43	4.17	1.01	76.39	11.35	2.20
20.79	QMB-28	18.67	145.64	99.25	9.78	53.06	19.37	146.42	146.18	25.35	145.55	14.86	9.32	178.10	4.08	0.95	37.61	10.97	1.79
21.54	QMB-29	21.15	155.05	130.46	25.94	82.29	19.52	108.73	243.22	33.34	215.46	18.21	6.32	168.94	5.90	1.20	7.87	13.96	2.17
22.28	QMB-30	15.89	112.47	117.65	24.10	68.12	16.96	74.93	228.09	31.20	215.81	14.48	4.34	131.15	5.76	0.93	9.51	11.93	2.00
23.02	QMB-31	16.03	122.56	154.35	16.37	64.51	17.45	89.86	218.63	33.05	305.50	19.20	4.61	227.58	8.06	1.27	7.88	13.64	2.45
23.76	QMB-32	23.19	181.26	128.38	23.22	80.46	20.44	156.18	159.45	28.75	185.59	16.10	8.92	202.12	5.08	1.19	9.56	13.65	2.07
24.51	QMB-33	12.70	87.27	85.17	27.83	80.79	14.96	54.66	179.80	23.49	176.15	9.02	3.02	119.29	4.68	0.72	8.92	8.86	1.50
25.25	QMB-34	16.83	141.91	124.55	23.81	88.03	18.86	122.35	220.81	28.81	245.20	15.29	7.33	215.05	6.58	1.11	41.27	14.13	2.19
25.99	QMB-35	15.70	118.18	102.21	16.32	59.22	18.58	120.41	206.12	26.43	191.25	13.70	6.83	198.65	5.08	1.00	77.42	12.30	1.92
26.74	QMB-36	16.99	137.22	126.35	19.85	71.38	19.62	129.06	267.41	32.84	252.92	19.61	7.17	215.95	6.77	1.25	105.04	14.95	2.98
27.48	QMB-37	14.80	106.35	86.60	15.83	58.19	18.07	108.93	146.43	25.04	167.72	14.62	5.90	206.58	4.58	0.98	7.50	11.55	1.68
28.22	QMB-38	19.93	149.12	110.87	14.78	64.92	19.49	169.62	146.33	25.63	169.05	16.65	9.52	292.31	4.68	1.09	9.70	12.91	2.16
29.04	QMB-39	6.62	57.04	82.28	12.32	39.39	14.46	43.85	125.87	20.64	227.79	7.28	2.34	159.00	5.71	0.59	17.97	7.84	1.60
40.33	QMB-40	11.86	93.01	93.33	12.56	46.36	16.92	82.88	162.24	24.70	253.22	10.45	9.39	252.72	6.66	0.84	98.46	11.30	2.72
41.16	QMB-41	11.52	86.78	85.22	14.03	48.71	15.80	81.24	154.57	24.59	199.12	9.73	4.69	214.86	5.29	0.78	38.48	9.97	1.80
42.80	QMB-42	17.07	126.45	94.31	29.69	83.42	18.62	134.22	135.98	24.54	162.26	12.37	8.11	362.45	4.57	0.94	40.99	11.81	1.78
44.74	QMB-43	11.94	101.90	106.55	16.23	53.67	16.83	76.70	147.88	24.34	175.94	12.83	4.36	176.29	4.90	0.85	8.56	9.34	1.67
46.39	QMB-44	13.76	117.87	104.70	13.89	54.44	17.06	89.04	137.06	24.09	177.28	14.29	5.07	213.77	4.78	0.91	17.40	9.94	1.65
48.03	QMB-45	12.57	111.54	107.26	14.80	55.13	17.01	81.84	144.94	24.90	179.70	14.26	4.68	169.27	4.79	0.94	33.58	10.12	1.69
49.68	QMB-46	13.30	109.06	96.22	16.13	56.84	16.93	86.40	132.20	22.74	158.16	11.56	4.91	169.02	4.20	0.82	8.06	9.14	1.53
51.33	QMB-47	13.90	109.88	99.11	18.69	51.36	16.85	89.74	136.39	23.17	171.35	11.48	5.13	202.48	4.57	0.78	26.64	9.35	1.55
52.97	QMB-48	15.32	131.12	107.29	17.02	63.95	18.00	108.85	140.97	25.18	192.70	13.37	6.46	200.84	5.19	0.95	8.74	10.88	1.83
54.62	QMB-49	14.35	124.90	92.21	12.58	52.35	17.38	102.63	114.43	21.84	156.92	12.81	5.81	186.71	4.21	0.85	28.97	9.64	1.55
56.26	QMB-50	13.81	120.00	102.64	10.85	50.24	17.25	99.70	132.71	22.97	183.57	13.83	5.63	174.06	5.11	0.90	67.13	10.39	1.72
57.91	QMB-51	13.65	125.70	99.83	15.08	51.95	17.54	104.66	117.63	22.28	169.56	15.53	5.73	180.87	4.78	0.90	19.97	10.19	1.76
59.55	QMB-52	14.82	131.62	107.24	11.45	53.14	17.86	111.89	112.03	21.98	184.32	13.76	6.21	191.04	5.09	0.92	17.80	10.53	1.79
61.19	QMB-53	16.62	151.83	121.32	10.96	58.12	19.72	131.82	123.08	27.20	209.48	16.18	7.24	237.55	5.75	1.08	54.57	12.56	2.18
62.84	QMB-54	14.00	116.75	107.01	16.04	56.06	17.39	97.59	127.26	24.39	199.65	12.37	5.24	178.96	5.47	0.85	44.93	9.97	1.67
64.49	QMB-55	17.32	133.88	99.46	15.96	57.69	17.97	118.91	109.45	24.26	159.81	14.02	6.90	222.16	4.34	0.93	18.38	10.53	1.65
66.14	QMB-56	18.97	163.32	107.65	27.90	70.25	19.39	144.61	77.02	24.47	163.48	44.75	8.33	356.94	4.50	1.17	72.66	11.56	3.29
67.78	QMB-57	12.22	96.01	101.29	13.75	39.57	17.49	77.91	122.08	28.56	291.38	14.87	4.05	282.37	7.49	0.96	64.61	11.88	2.26
69.43	QMB-58	11.64	83.67	102.74	10.76	36.23	16.74	67.21	120.13	29.85	338.17	13.70	3.52	219.44	8.66	0.87	11.05	11.01	1.99
71.07	QMB-59	11.63	94.62	105.32	11.42	41.51	16.59	74.86	105.51	29.49	296.00	14.91	4.21	314.42	7.66	0.96	66.71	11.59	2.18
72.72	QMB-60	12.18	96.32	87.58	10.04	44.44	16.76	75.49	136.48	27.56	229.85	12.54	4.34	305.12	5.82	0.83	26.84	10.25	1.76
74.36	QMB-61	12.00	97.80	97.82	12.50	50.26	17.19	74.69	89.21	27.04	250.66	12.99	4.16	317.54	6.52	0.91	29.89	11.14	1.96
75.19	QMB-62	11.61	80.60	117.76	12.34	42.33	16.33	46.14	82.92	28.45	449.93	12.39	2.47	229.06	11.63	0.89	12.92	10.97	2.13
76.01	QMB-63	8.29	59.39	94.05	10.55	37.63	13.89	37.01	86.46	29.09	469.03	8.35	2.06	231.97	11.88	0.62	9.47	8.35	1.67
76.83	QMB-64	9.81	66.53	105.46	13.36	45.89	14.75	43.27	93.89	30.78	553.18	9.58	2.41	208.48	14.20	0.77	12.44	13.02	2.35
77.65	QMB-65	10.50	78.92	82.75	10.89	45.10	15.57	58.62	72.61	24.18	259.37	9.62	3.07	217.04	6.64	0.74	29.90	9.36	1.73
78.48	QMB-66	17.02	151.26	100.69	16.99	66.95	18.66	114.74	166.05	22.28	145.53	12.31	6.29	137.95	3.91	0.86	13.83	10.26	1.89

Table 3. Rare Earth Elements REE of the Qumiba section

Depth (m)	Sample	La	Ce	Pr	Nd	Sm	Eu	Gd	Tb	Dy	Ho	Er	Tm	Yb	Lu	Y
0.74	QMB-1	0.52	0.55	0.62	0.67	0.84	0.98	0.74	0.77	0.92	0.90	0.68	0.87	0.86	0.88	1.02
1.49	QMB-2	0.94	0.97	0.99	1.03	1.17	1.36	0.95	0.95	1.19	1.18	0.87	1.19	1.15	1.18	1.34
2.23	QMB-3	0.68	0.70	0.72	0.74	0.77	0.89	0.61	0.67	0.82	0.81	0.63	0.84	0.81	0.86	0.92
2.97	QMB-4	0.81	0.85	0.85	0.87	0.91	1.07	0.73	0.75	0.97	0.96	0.70	0.94	0.94	1.00	1.06
3.71	QMB-5	0.80	0.84	0.85	0.83	0.92	1.08	0.77	0.82	0.96	0.96	0.76	1.00	0.94	1.00	1.08
4.46	QMB-6	0.75	0.78	0.78	0.80	0.87	1.01	0.84	0.86	0.94	0.94	0.79	0.91	0.89	0.90	1.07
5.20	QMB-7	0.72	0.75	0.75	0.78	0.85	0.98	0.76	0.81	0.93	0.95	0.74	0.91	0.90	0.93	1.05
5.94	QMB-8	0.29	0.36	0.41	0.46	0.62	0.73	0.71	0.75	0.75	0.73	0.60	0.64	0.59	0.62	0.85
6.68	QMB-9	0.47	0.50	0.56	0.61	0.78	0.91	0.79	0.82	0.87	0.86	0.68	0.76	0.74	0.77	0.97
7.43	QMB-10	0.69	0.73	0.73	0.77	0.85	0.95	0.81	0.85	0.90	0.91	0.75	0.85	0.82	0.92	1.02
8.17	QMB-11	0.55	0.60	0.62	0.66	0.73	0.86	0.75	0.81	0.86	0.85	0.72	0.80	0.75	0.86	0.98
8.91	QMB-12	0.64	0.67	0.69	0.73	0.81	0.93	0.79	0.83	0.90	0.91	0.76	0.88	0.86	0.90	1.03
9.65	QMB-13	0.82	0.78	0.77	0.78	0.80	0.91	0.77	0.81	0.85	0.87	0.78	0.91	0.82	0.90	0.97
10.40	QMB-14	0.84	0.83	0.83	0.86	0.93	0.99	0.87	0.90	0.88	0.92	0.88	0.93	0.91	1.01	1.02
11.14	QMB-15	0.77	0.80	0.79	0.84	0.90	1.07	0.93	0.93	0.91	0.91	0.85	0.88	0.84	0.89	1.01
11.88	QMB-16	0.67	0.72	0.72	0.76	0.90	1.01	0.91	0.92	0.86	0.87	0.77	0.78	0.78	0.85	0.92
12.62	QMB-17	0.63	0.66	0.67	0.70	0.79	0.89	0.80	0.83	0.83	0.85	0.79	0.82	0.80	0.84	0.94
13.37	QMB-18	0.64	0.65	0.67	0.69	0.77	0.86	0.74	0.79	0.78	0.79	0.72	0.77	0.76	0.78	0.88
14.11	QMB-19	0.67	0.70	0.69	0.72	0.79	0.87	0.84	0.88	0.81	0.79	0.76	0.77	0.74	0.78	0.87
14.85	QMB-20	0.66	0.71	0.72	0.76	0.83	0.93	0.87	0.90	0.86	0.87	0.83	0.86	0.80	0.87	0.92
15.60	QMB-21	0.70	0.76	0.75	0.79	0.85	0.98	0.92	0.96	0.90	0.91	0.86	0.88	0.85	0.92	0.97
16.34	QMB-22	0.62	0.69	0.72	0.75	0.84	0.97	0.89	0.91	0.85	0.86	0.80	0.83	0.78	0.81	0.91
17.08	QMB-23	0.68	0.76	0.76	0.79	0.87	0.98	0.89	0.91	0.89	0.89	0.85	0.88	0.82	0.91	0.96
17.82	QMB-24	0.62	0.70	0.70	0.74	0.83	0.98	0.91	0.92	0.87	0.85	0.82	0.82	0.79	0.84	0.94
19.31	QMB-26	0.63	0.70	0.71	0.74	0.81	0.97	0.90	0.92	0.88	0.87	0.83	0.84	0.80	0.84	0.94
20.05	QMB-27	0.66	0.72	0.75	0.79	0.89	1.02	1.01	0.99	0.91	0.90	0.87	0.85	0.81	0.83	0.98
20.79	QMB-28	0.61	0.69	0.69	0.72	0.80	0.91	0.83	0.87	0.81	0.84	0.81	0.78	0.78	0.81	0.93
21.54	QMB-29	0.91	0.92	0.92	0.98	1.16	0.97	0.89	0.79	0.81	0.78	0.70	1.05	1.01	1.05	1.22
22.28	QMB-30	0.67	0.72	0.75	0.82	0.95	0.92	0.81	0.75	0.76	0.74	0.67	0.93	0.91	0.93	1.14
23.02	QMB-31	0.90	0.83	0.87	0.92	1.06	0.92	0.84	0.76	0.79	0.75	0.68	1.11	1.02	1.04	1.21
23.76	QMB-32	0.88	0.89	0.89	0.95	1.01	0.91	0.83	0.78	0.77	0.76	0.68	0.96	0.95	0.94	1.05
24.51	QMB-33	0.52	0.58	0.60	0.66	0.78	0.80	0.71	0.71	0.69	0.70	0.63	0.68	0.69	0.68	0.86
25.25	QMB-34	0.85	0.83	0.83	0.86	0.95	0.76	0.80	0.77	0.75	0.77	0.67	1.01	0.99	0.99	1.06
25.99	QMB-35	0.73	0.77	0.78	0.80	0.89	0.90	0.79	0.79	0.77	0.77	0.70	0.89	0.88	0.88	0.97
26.74	QMB-36	0.95	0.96	0.94	0.97	1.07	1.14	0.89	0.80	0.81	0.75	0.70	1.07	1.09	1.12	1.20
27.48	QMB-37	0.69	0.74	0.72	0.77	0.83	0.87	0.74	0.77	0.74	0.74	0.68	0.83	0.83	0.84	0.92
28.22	QMB-38	0.73	0.74	0.72	0.74	0.80	0.86	0.74	0.77	0.74	0.73	0.67	0.89	0.89	0.92	0.94
29.04	QMB-39	0.42	0.46	0.47	0.50	0.60	0.69	0.65	0.72	0.68	0.72	0.64	0.65	0.63	0.69	0.76
40.33	QMB-40	0.72	0.68	0.68	0.71	0.78	0.83	0.73	0.75	0.73	0.73	0.66	0.86	0.84	0.89	0.90
41.16	QMB-41	0.64	0.64	0.66	0.70	0.77	0.88	0.72	0.71	0.70	0.69	0.63	0.81	0.80	0.82	0.90
42.80	QMB-42	0.69	0.70	0.69	0.72	0.78	0.89	0.73	0.75	0.73	0.73	0.67	0.86	0.81	0.83	0.90
44.74	QMB-43	0.58	0.64	0.65	0.68	0.81	0.88	0.74	0.75	0.73	0.73	0.67	0.79	0.77	0.78	0.89
46.39	QMB-44	0.63	0.67	0.67	0.70	0.80	0.90	0.73	0.74	0.72	0.71	0.65	0.80	0.75	0.81	0.88
48.03	QMB-45	0.61	0.67	0.68	0.71	0.82	0.88	0.75	0.75	0.73	0.73	0.66	0.81	0.77	0.79	0.91
49.68	QMB-46	0.56	0.62	0.64	0.66	0.78	0.84	0.71	0.74	0.71	0.72	0.66	0.74	0.70	0.75	0.83
51.33	QMB-47	0.56	0.60	0.62	0.66	0.75	0.87	0.71	0.75	0.72	0.73	0.66	0.75	0.70	0.74	0.85
52.97	QMB-48	0.66	0.70	0.71	0.76	0.83	0.91	0.75	0.76	0.74	0.74	0.67	0.82	0.83	0.84	0.92
54.62	QMB-49	0.63	0.64	0.63	0.68	0.71	0.79	0.70	0.75	0.71	0.73	0.66	0.73	0.69	0.72	0.80
56.26	QMB-50	0.63	0.67	0.68	0.72	0.82	0.80	0.73	0.75	0.72	0.74	0.66	0.82	0.77	0.81	0.84
57.91	QMB-51	0.66	0.68	0.68	0.70	0.77	0.77	0.70	0.75	0.71	0.73	0.66	0.78	0.71	0.75	0.82
59.55	QMB-52	0.66	0.68	0.67	0.70	0.78	0.81	0.70	0.75	0.71	0.73	0.66	0.81	0.74	0.81	0.80
61.19	QMB-53	0.85	0.86	0.84	0.87	0.88	0.96	0.79	0.81	0.78	0.77	0.71	0.94	0.91	0.95	1.00
62.84	QMB-54	0.62	0.66	0.65	0.69	0.79	0.88	0.72	0.75	0.72	0.73	0.66	0.78	0.79	0.81	0.89
64.49	QMB-55	0.67	0.71	0.70	0.74	0.80	0.91	0.73	0.75	0.72	0.73	0.66	0.79	0.78	0.77	0.89
66.14	QMB-56	0.77	0.79	0.76	0.83	0.87	0.86	0.76	0.77	0.74	0.75	0.67	0.85	0.80	0.83	0.90
67.78	QMB-57	0.84	0.81	0.81	0.83	0.80	0.93	0.77	0.78	0.76	0.74	0.69	0.95	0.89	0.96	1.05
69.43	QMB-58	0.71	0.74	0.76	0.79	0.84	0.87	0.76	0.77	0.75	0.74	0.68	0.93	0.84	0.88	1.09
71.07	QMB-59	0.79	0.80	0.83	0.86	0.86	0.99	0.86	0.90	0.90	0.95	0.89	0.96	0.93	0.99	1.08
72.72	QMB-60	0.70	0.72	0.74	0.77	0.87	1.00	0.86	0.90	0.87	0.87	0.78	0.83	0.80	0.83	1.01
74.36	QMB-61	0.68	0.70	0.72	0.75	0.80	0.96	0.79	0.85	0.85	0.87	0.81	0.87	0.86	0.91	0.99
75.19	QMB-62	0.64	0.67	0.69	0.69	0.73	0.95	0.74	0.79	0.78	0.82	0.78	0.86	0.85	0.91	1.04
76.01	QMB-63	0.43	0.48	0.52	0.58	0.76	0.97	0.79	0.81	0.78	0.76	0.68	0.71	0.70	0.77	1.07
76.83	QMB-64	0.61	0.63	0.65	0.69	0.80	0.93	0.83	0.88	0.87	0.87	0.81	0.89	0.88	0.96	1.13
77.65	QMB-65	0.54	0.57	0.59	0.61	0.67	0.87	0.71	0.77	0.77	0.77	0.70	0.77	0.74	0.80	0.89
78.48	QMB-66	0.64	0.66	0.66	0.68	0.74	0.90	0.74	0.77	0.74	0.75	0.68	0.74	0.71	0.75	0.82

Table 4. Carbon Isotopes of Qumiba 1-30 samples

Identifier 1	Depth (m)	Sample Number	d13C 2-pt w/ lin corr
QMB 2	1.49	2	-29.67
QMB 3	2.23	3	-29.96
QMB 4	2.97	4	-28.96
QMB 5	3.71	5	-28.80
QMB 6	4.46	6	-29.03
QMB 7	5.20	7	27.70
QMB 9	6.68	9	-25.39
QMB 10	7.43	10	-29.14
QMB 11	8.17	11	-27.19
QMB 12	8.91	12	-29.03
QMB 13	9.65	13	-29.48
QMB 14	10.40	14	-29.72
QMB 15	11.14	15	-28.89
QMB 16	11.88	16	-29.97
QMB 17	12.62	17	-28.55
QMB 18	13.37	18	-28.63
QMB 19	14.11	19	-30.06
QMB 20	14.85	20	-33.79
QMB 21	15.60	21	-26.44
QMB 22	16.34	22	-31.41
QMB 23	17.08	23	-30.45
QMB 24	17.82	24	-28.86
QMB 25	18.57	25	-27.55
QMB 26	19.31	26	-31.48
QMB 27	20.05	27	-29.61
QMB 28	20.79	28	-28.57
QMB 29	21.54	29	-30.68
QMB 30	22.28	30	-30.25

Excluded samples	Depth (m)	Sample number	d13C 2-pt w/ lin corr
QMB 1	0.74	1	-23.35
QMB 8	5.94	8	-22.15

Table 5. Nitrogen Isotopes of Qumiba 1-30 samples

Identifier 1	Depth (m)	Sample Number	d15N 2-pt w/ lin corr
QMB 2	1.49	2	4.56
QMB 3	2.23	3	5.17
QMB 4	2.97	4	5.41
QMB 5	3.71	5	5.51
QMB 6	4.46	6	4.93
QMB 7	5.20	7	5.03
QMB 10	7.43	10	4.97
QMB 11	8.17	11	4.89
QMB 12	8.91	12	4.76
QMB 13	9.65	13	5.29
QMB 14	10.40	14	6.23
QMB 15	11.14	15	5.87
QMB 16	11.88	16	5.44
QMB 17	12.62	17	5.54
QMB 18	13.37	18	5.86
QMB 19	14.11	19	6.58
QMB 20	14.85	20	6.13
QMB 21	15.60	21	6.70
QMB 22	16.34	22	5.05
QMB 23	17.08	23	5.87
QMB 24	17.82	24	5.72
QMB 25	18.57	25	5.72
QMB 26	19.31	26	5.49
QMB 27	20.05	27	6.99
QMB 28	20.79	28	7.04
QMB 29	21.54	29	4.79
QMB 30	22.28	30	5.29

7 References

Aitchison, J.C., Xia, X., Baxter, A.T. and Ali, J.R., 2011. Detrital zircon U–Pb ages along the Yarlung-Tsangpo suture zone, Tibet: implications for oblique convergence and collision between India and Asia. Gondwana Research, 20(4): 691-709.

Altabet, M.A., 2006. Isotopic tracers of the marine nitrogen cycle: present and past, Marine organic matter: biomarkers, isotopes and DNA. Springer, pp. 251-293.

Anagnostou, E., Sherrell, R.M., Gagnon, A., LaVigne, M., Field, M.P. and McDonough, W.F., 2011. Seawater nutrient and carbonate ion concentrations recorded as P/Ca, Ba/Ca, and U/Ca in the deep-sea coral Desmophyllum dianthus. Geochimica et Cosmochimica Acta, 75(9): 2529-2543.

Ando, A., Kakegawa, T., Takashima, R. and Saito, T., 2002. New perspective on Aptian carbon isotope stratigraphy: data from δ13C records of terrestrial organic matter. Geology, 30(3): 227-230.

Andrews, J., Greenaway, A. and Dennis, P., 1998. Combined carbon isotope and C/N ratios as indicators of source and fate of organic matter in a poorly flushed, tropical estuary: Hunts Bay, Kingston Harbour, Jamaica. Estuarine, Coastal and Shelf Science, 46(5): 743-756.

Arthur, M.A., Dean, W.E. and Claypool, G.E., 1985. Anomalous ^{13}C enrichment in modern marine organic carbon. Nature, 315(16): 216-218.

Bahlburg, H. and Dobrzinski, N., 2011. A review of the Chemical Index of Alteration (CIA) and its application to the study of Neoproterozoic glacial deposits and climate transitions. Geological Society, London, Memoirs, 36(1): 81-92.

Bau, M. and Dulski, P., 1996. Distribution of yttrium and rare-earth elements in the Penge and Kuruman iron-formations, Transvaal Supergroup, South Africa. Precambrian Research, 79(1-2): 37-55.

Berger, W., Smetacek, V. and Wefer, G., 1989. Ocean productivity and paleoproductivity—an overview, Productivity of the ocean: present and past. Wiley New York, pp. 1-34.

Bhatia, M.R. and Crook, K.A., 1986. Trace element characteristics of graywackes and tectonic setting discrimination of sedimentary basins. Contributions to mineralogy and petrology, 92(2): 181-193.

Cai, F., Ding, L. and Yue, Y., 2011. Provenance analysis of upper Cretaceous strata in the Tethys Himalaya, southern Tibet: implications for timing of India–Asia collision. Earth and Planetary Science Letters, 305(1-2): 195-206.

Caves, J.K., Jost, A.B., Lau, K.V. and Maher, K., 2016. Cenozoic carbon cycle imbalances and a variable weathering feedback. Earth and Planetary Science Letters, 450: 152-163.

Cullers, R.L., 2002. Implications of elemental concentrations for provenance, redox conditions, and metamorphic studies of shales and limestones near Pueblo, CO, USA. Chemical Geology, 191(4): 305-327.

Cullers, R.L., Basu, A. and Suttner, L.J., 1988. Geochemical signature of provenance in sand-size material in soils and stream sediments near the Tobacco Root batholith, Montana, USA. Chemical Geology, 70(4): 335-348.

Dähnke, K. and Thamdrup, B., 2013. Nitrogen isotope dynamics and fractionation during sedimentary denitrification in Boknis Eck, Baltic Sea. Biogeosciences (BG), 10(5): 3079-3088.

Dean, W.E., Arthur, M.A. and Claypool, G.E., 1986. Depletion of ^{13}C in Cretaceous marine organic matter: Source, diagenetic, or environmental sigal? Marine Geology, 70(1): 119-157.

Deutsch, C., Sigman, D.M., Thunell, R.C., Meckler, A.N. and Haug, G.H., 2004. Isotopic constraints on glacial/interglacial changes in the oceanic nitrogen budget. Global Biogeochemical Cycles, 18(4).

Diefendorf, A.F., Mueller, K.E., Wing, S.L., Koch, P.L. and Freeman, K.H., 2010. Global patterns in leaf ^{13}C discrimination and implications for studies of past and future climate. Proceedings of

the National Academy of Sciences, 107(13): 5738-5743.
Dietzel, M., Gussone, N. and Eisenhauer, A., 2004. Co-precipitation of Sr2+ and Ba2+ with aragonite by membrane diffusion of CO2 between 10 and 50 C. Chemical Geology, 203(1-2): 139-151.
Ding, L., Qasim, M., Jadoon, I.A., Khan, M.A., Xu, Q., Cai, F., Wang, H., Baral, U. and Yue, Y., 2016. The India–Asia collision in north Pakistan: Insight from the U–Pb detrital zircon provenance of Cenozoic foreland basin. Earth and Planetary Science Letters, 455: 49-61.
Dymond, J., Suess, E. and Lyle, M., 1992. Barium in deep‐sea sediment: A geochemical proxy for paleoproductivity. Paleoceanography, 7(2): 163-181.
Erbacher, J., Friedrich, O., Wilson, P.A., Birch, H. and Mutterlose, J., 2005. Stable organic carbon isotope stratigraphy across Oceanic Anoxic Event 2 of Demerara Rise, western tropical Atlantic. Geochemistry, Geophysics, Geosystems, 6(6).
Fedo, C.M., Wayne Nesbitt, H. and Young, G.M., 1995. Unraveling the effects of potassium metasomatism in sedimentary rocks and paleosols, with implications for paleoweathering conditions and provenance. Geology, 23(10): 921-924.
Floyd, P. and Leveridge, B., 1987. Tectonic environment of the Devonian Gramscatho basin, south Cornwall: framework mode and geochemical evidence from turbiditic sandstones. Journal of the Geological Society, 144(4): 531-542.
Galimov, E.M., 1985. The biological fractionation of isotopes. Academic press.
Garzanti, E., Padoan, M., Setti, M., López-Galindo, A. and Villa, I.M., 2014. Provenance versus weathering control on the composition of tropical river mud (southern Africa). Chemical Geology, 366: 61-74.
German, C.R. and Elderfield, H., 1990. Application of the Ce anomaly as a paleoredox indicator: the ground rules. Paleoceanography, 5(5): 823-833.
Gingele, F., Zabel, M., Kasten, S., Bonn, W. and Nürnberg, C., 1999. Biogenic barium as a proxy for paleoproductivity: Methods and limitations of application, Use of Proxies in Paleoceanography. Springer, pp. 345-364.
Goldberg, K. and Humayun, M., 2010. The applicability of the Chemical Index of Alteration as a paleoclimatic indicator: An example from the Permian of the Paraná Basin, Brazil. Palaeogeography, Palaeoclimatology, Palaeoecology, 293(1-2): 175-183.
Gromet, L.P., Haskin, L.A., Korotev, R.L. and Dymek, R.F., 1984. The "North American shale composite": its compilation, major and trace element characteristics. Geochimica et Cosmochimica Acta, 48(12): 2469-2482.
Gu, X., Liu, J., Zheng, M., Tang, J. and Qi, L., 2002. Provenance and tectonic setting of the Proterozoic turbidites in Hunan, South China: geochemical evidence. Journal of sedimentary Research, 72(3): 393-407.
Harnois, L., 1988. The CIW index: a new chemical index of weathering. Sedimentary geology, 55: 319-322.
Hayes, J.M., Strauss, H. and Kaufman, A.J., 1999. The abundance of ^{13}C in marine organic matter and isotopic fractionation in the global biogeochemical cycle of carbon during the past 800 Ma. Chemical Geology, 161(1-3): 103-125.
Hedges, J.I. and Parker, P.L., 1976. Land-derived organic matter in surface sediments from the Gulf of Mexico. Geochimica et Cosmochimica Acta, 40(9): 1019-1029.
Hu, X., Garzanti, E., Wang, J., Huang, W., An, W. and Webb, A., 2016. The timing of India-Asia collision onset–Facts, theories, controversies. Earth-Science Reviews, 160: 264-299.
Hu, X., Sinclair, H.D., Wang, J., Jiang, H. and Wu, F., 2012. Late Cretaceous-Palaeogene stratigraphic and basin evolution in the ZhepureMountain of southern Tibet: implications for the timing of India-Asia initial collision. Basin Research, 24(5): 520-543.
Jacot Des Combes, H., Esper, O., De La Rocha, C., Abelmann, A., Gersonde, R., Yam, R. and Shemesh, A., 2008. Diatom δ13C, δ15N, and C/N since the Last Glacial Maximum in the Southern Ocean: Potential impact of species composition. Paleoceanography, 23(4).
Jiang, T., Aitchison, J.C. and Wan, X., 2016. The youngest marine deposits preserved in southern

Tibet and disappearance of the Tethyan Ocean. Gondwana Research, 32: 64-75.
Kahsnitz, M., 2017. Paleocene to Lower Eocene sediments of the eastern Neo-Tethyan Ocean: sedimentary and geodynamic evolution as well as biostratigraphy of the larger benthic foraminifera Lockhartia and the genesis of nodular limestones, Universität Bremen.
Kashiyama, Y., Ogawa, N., Kuroda, J., Shiro, M., Nomoto, S., Tada, R., Kitazato, H. and Ohkouchi, N., 2008. Diazotrophic cyanobacteria as the major photoautotrophs during mid-Cretaceous oceanic anoxic events: Nitrogen and carbon isotopic evidence from sedimentary porphyrin. Organic Geochemistry, 39(5): 532-549.
Kast, E.R., Stolper, D.A., Auderset, A., Higgins, J.A., Ren, H., Wang, X.T., Martínez-García, A., Haug, G.H. and Sigman, D.M., 2019. Nitrogen isotope evidence for expanded ocean suboxia in the early Cenozoic. Science, 364(6438): 386-389.
Kritee, K., Sigman, D.M., Granger, J., Ward, B.B., Jayakumar, A. and Deutsch, C., 2012. Reduced isotope fractionation by denitrification under conditions relevant to the ocean. Geochimica et Cosmochimica Acta, 92: 243-259.
Kump, L.R. and Arthur, M.A., 1997. Global chemical erosion during the Cenozoic: Weatherability balances the budgets, Tectonic Uplift and Climate Change. Springer, pp. 399-426.
Large, R.R., Halpin, J.A., Danyushevsky, L.V., Maslennikov, V.V., Bull, S.W., Long, J.A., Gregory, D.D., Lounejeva, E., Lyons, T.W. and Sack, P.J., 2014. Trace element content of sedimentary pyrite as a new proxy for deep-time ocean–atmosphere evolution. Earth and Planetary Science Letters, 389: 209-220.
Li, C. and Yang, S., 2010. Is chemical index of alteration (CIA) a reliable proxy for chemical weathering in global drainage basins? American Journal of Science, 310(2): 111-127.
Mackensen, A. and Schmiedl, G., 2019. Stable carbon isotopes in paleoceanography: Atmosphere, oceans, and sediments. Earth-Science Reviews: 102893.
McLennan, S., Hemming, S., McDaniel, D. and Hanson, G., 1993. Geochemical approaches to sedimentation, provenance, and tectonics. Special Papers-Geological Society of America: 21-21.
McLennan, S.M., 1989. Rare earth elements in sedimentary rocks: influence of provenance and sedimentary processes. Geochemistry and Mineralogy of Rare Earth Elements, Reviews in Mineralogy 21: 169-200.
Meunier, A., Caner, L., Hubert, F., El Albani, A. and Prêt, D., 2013. The weathering intensity scale (WIS): an alternative approach of the chemical index of alteration (CIA). American Journal of Science, 313(2): 113-143.
Miller, K.G., Browning, J.V., Schmelz, W.J., Kopp, R.E., Mountain, G.S. and Wright, J.D., 2020. Cenozoic sea-level and cryospheric evolution from deep-sea geochemical and continental margin records. Science Advances, 6(20): eaaz1346.
Montoya, J.P., 1994. Nitrogen isotope fractionation in the modern ocean: implications for the sedimentary record, Carbon cycling in the glacial ocean: constraints on the ocean's role in global change. Springer, pp. 259-279.
Murray, R.W., Buchholtz ten Brink, M.R., Jones, D.L., Gerlach, D.C. and Russ III, G.P., 1990. Rare earth elements as indicators of different marine depositional environments in chert and shale. Geology, 18(3): 268-271.
Najman, Y., Appel, E., Boudagher‐Fadel, M., Bown, P., Carter, A., Garzanti, E., Godin, L., Han, J., Liebke, U. and Oliver, G., 2010. Timing of India‐Asia collision: Geological, biostratigraphic, and palaeomagnetic constraints. Journal of Geophysical Research: Solid Earth, 115(B12).
Najman, Y., Jenks, D., Godin, L., Boudagher-Fadel, M., Millar, I., Garzanti, E., Horstwood, M. and Bracciali, L., 2017. The Tethyan Himalayan detrital record shows that India–Asia terminal collision occurred by 54 Ma in the Western Himalaya. Earth and Planetary Science Letters, 459: 301-310.

Nesbitt, H. and Young, G., 1982. Early Proterozoic climates and plate motions inferred from major element chemistry of lutites. Nature, 299(5885): 715.
Nicolo, M.J., Dickens, G.R., Hollis, C.J. and Zachos, J.C., 2007. Multiple early Eocene hyperthermals: Their sedimentary expression on the New Zealand continental margin and in the deep sea. Geology, 35(8): 699-702.
Parker, A., 1970. An index of weathering for silicate rocks. Geological Magazine, 107(6): 501-504.
Paytan, A., Kastner, M. and Chavez, F., 1996. Glacial to interglacial fluctuations in productivity in the equatorial Pacific as indicated by marine barite. Science, 274(5291): 1355-1357.
Peters, K., Sweeney, R. and Kaplan, I., 1978. Correlation of carbon and nitrogen stable isotope ratios in sedimentary organic matter. Limnology and Oceanography, 23(4): 598-604.
Popp, B., Parekh, P., Tilbrook, B., Bidigare, R. and Laws, E., 1997. Organic carbon δ13C variations in sedimentary rocks as chemostratigraphic and paleoenvironmental tools. Palaeogeography, Palaeoclimatology, Palaeoecology, 132(1-4): 119-132.
Rau, G.H., Arthur, M.A. and Dean, W.E., 1987. 15N/14N variations in Cretaceous Atlantic sedimentary sequences: implication for past changes in marine nitrogen biogeochemistry. Earth and Planetary Science Letters, 82(3-4): 269-279.
Raymo, M. and Ruddiman, W., 1992. Tectonic forcing of late Cenozoic climate. Nature, 359(6391): 117-122.
Rowley, D.B., 1996. Age of initiation of collision between India and Asia: A review of stratigraphic data. Earth and Planetary Science Letters, 145(1-4): 1-13.
Ruhl, M., Kürschner, W.M. and Krystyn, L., 2009. Triassic–Jurassic organic carbon isotope stratigraphy of key sections in the western Tethys realm (Austria). Earth and Planetary Science Letters, 281(3-4): 169-187.
Sackett, W.M., 1964. The depositional history and isotopic organic carbon composition of marine sediments. Marine Geology, 2(3): 173-185.
Schoeninger, M.J. and DeNiro, M.J., 1984. Nitrogen and carbon isotopic composition of bone collagen from marine and terrestrial animals. Geochimica et Cosmochimica Acta, 48(4): 625-639.
Searle, M., Windley, B., Coward, M., Cooper, D., Rex, A., Rex, D., Tingdong, L., Xuchang, X., Jan, M. and Thakur, V., 1987. The closing of Tethys and the tectonics of the Himalaya. Geological Society of America Bulletin, 98(6): 678-701.
Shao, J., Yang, S. and Li, C., 2012. Chemical indices (CIA and WIP) as proxies for integrated chemical weathering in China: inferences from analysis of fluvial sediments. Sedimentary Geology, 265: 110-120.
Sigman, D. and Haug, G., 2003. The biological pump in the past. Treatise on geochemistry, 6: 491-528.
Sigman, D., Karsh, K. and Casciotti, K., 2009. Ocean process tracers: nitrogen isotopes in the ocean. Encyclopedia of ocean science, 2nd edn Elsevier, Amsterdam.
Singh, B., 2013. Evolution of the Paleogene succession of the western Himalayan foreland basin. Geoscience Frontiers, 4(2): 199-212.
Slotnick, B.S., Dickens, G.R., Nicolo, M.J., Hollis, C.J., Crampton, J.S., Zachos, J.C. and Sluijs, A., 2012. Large-amplitude variations in carbon cycling and terrestrial weathering during the latest Paleocene and earliest Eocene: the record at Mead Stream, New Zealand. The journal of geology, 120(5): 487-505.
Spicer, R.A., Su, T., Valdes, P.J., Farnsworth, A., Wu, F.-X., Shi, G., Spicer, T.E. and Zhou, Z., 2020. Why the 'Uplift of the Tibetan Plateau'is a myth. National Science Review.
Talbot, M.R., 2002. Nitrogen isotopes in palaeolimnology, Tracking environmental change using lake sediments. Springer, pp. 401-439.
Tribovillard, N., Algeo, T., Lyons, T. and Riboulleau, A., 2006. Trace metals as paleoredox and paleoproductivity proxies: An update. Chemical Geology, 232(1-2): 12-32.
Tyson, R.V., 1995. Bulk geochemical characterization and classification of organic matter: Stable

carbon isotopes (δ 13 C), Sedimentary organic matter. Springer, pp. 395-416.
van Hinsbergen, D.J.J., Lippert, P.C., Dupont-Nivet, G., McQuarrie, N., Doubrovine, P.V., Spakman, W. and Torsvik, T.H., 2012. Greater India Basin hypothesis and a two-stage Cenozoic collision between India and Asia. Proceedings of the National Academy of Sciences, 109(20): 7659-7664.
Wan, X., Jiang, T., Zhang, Y., Xi, D. and Li, G., 2014. Palaeogene marine stratigraphy in C hina. Lethaia, 47(3): 297-308.
Wang, C., Li, X., Hu, X. and Jansa, L., 2002. Latest marine horizon north of Qomolangma (Mt Everest): Implications for closure of Tethys seaway and collision tectonics. Terra Nova, 14(2): 114-120.
Wang, C., Li, X., Liu, Z., Li, Y., Jansa, L., Dai, J. and Wei, Y., 2012. Revision of the Cretaceous–Paleogene stratigraphic framework, facies architecture and provenance of the Xigaze forearc basin along the Yarlung Zangbo suture zone. Gondwana Research, 22(2): 415-433.
Wang, C., Zhao, X., Liu, Z., Lippert, P.C., Graham, S.A., Coe, R.S., Yi, H., Zhu, L., Liu, S. and Li, Y., 2008. Constraints on the early uplift history of the Tibetan Plateau. Proceedings of the National Academy of Sciences, 105(13): 4987-4992.
Wang, P., Du, Y., Yu, W., Algeo, T.J., Zhou, Q., Xu, Y., Qi, L., Yuan, L. and Pan, W., 2019. The chemical index of alteration (CIA) as a proxy for climate change during glacial-interglacial transitions in Earth history. Earth-Science Reviews: 103032.
Wang, Z., Wang, J., Fu, X., Zhan, W., Yu, F., Feng, X., Song, C., Chen, W. and Zeng, S., 2017. Organic material accumulation of Carnian mudstones in the North Qiangtang Depression, eastern Tethys: controlled by the paleoclimate, paleoenvironment, and provenance. Marine and Petroleum Geology, 88: 440-457.
Waser, N., Harrison, P., Nielsen, B., Calvert, S. and Turpin, D., 1998. Nitrogen isotope fractionation during the uptake and assimilation of nitrate, nitrite, ammonium, and urea by a marine diatom. Limnology and Oceanography, 43(2): 215-224.
Webb, G.E. and Kamber, B.S., 2000. Rare earth elements in Holocene reefal microbialites: a new shallow seawater proxy. Geochimica et Cosmochimica Acta, 64(9): 1557-1565.
Willems, H., Zhou, Z., Zhang, B.-g. and Gräfe, K.-U., 1996. Stratigraphy of the Upper Cretaceous and lower Tertiary strata in the Tethyan Himalayas of Tibet (Tingri area, China). Geologische Rundschau, 85(4): 723.
Yang, J., Cawood, P.A., Montañez, I.P., Condon, D.J., Du, Y., Yan, J.-X., Yan, S. and Yuan, D., 2020. Enhanced continental weathering and large igneous province induced climate warming at the Permo-Carboniferous transition. Earth and Planetary Science Letters, 534: 116074.
Yin, A. and Harrison, T.M., 2000. Geologic evolution of the Himalayan-Tibetan orogen. Annual Review of Earth and Planetary Sciences, 28(1): 211-280.
Zhang, Q., Willems, H. and Ding, L., 2013. Evolution of the Paleocene-Early Eocene larger benthic foraminifera in the Tethyan Himalaya of Tibet, China. International Journal of Earth Sciences, 102(5): 1427-1445.
Zhang, Q., Willems, H., Ding, L., Gräfe, K.-U. and Appel, E., 2012. Initial India-Asia continental collision and foreland basin evolution in the Tethyan Himalaya of Tibet: Evidence from stratigraphy and paleontology. The Journal of Geology, 120(2): 175-189.
Zhu, B., Kidd, W.S., Rowley, D.B., Currie, B.S. and Shafique, N., 2005. Age of initiation of the India-Asia collision in the east-central Himalaya. The Journal of Geology, 113(3): 265-285.
Zhu, C., Meng, J., Hu, Y., Wang, C. and Zhang, J., 2019. East‐Central Asian climate evolved with the northward migration of the high proto‐Tibetan Plateau. Geophysical Research Letters, 46(14): 8397-8406.